



Cite this: DOI: 10.1039/d0nj03301d

Experimental and theoretical study of bidirectional photoswitching behavior of 5,5'-diphenylhydantoin Schiff bases: synthesis, crystal structure and kinetic approaches†

 Petar Todorov,^a Stela Georgieva,^b Petia Peneva,^{ac} Rusi Rusew,^c Boris Shivachev^c and Anton Georgiev^{ad}

Herein, the synthesis and characterization of four novel 5,5'-diphenylhydantoin Schiff bases containing different aromatic species are presented. Their structure–property relationship was studied by X-ray, optical and electrochemical methods as well as DFT calculations in terms of their *E/Z* photoisomerization and enol/keto phototautomerization. The big challenge in photoinduced motion is achieving control and stability over the two isomers. Solvent-driven bidirectional photoswitching behavior was studied in nonpolar 1,4-dioxane and polar aprotic DMF. T-type photochromism in 1,4-DOX and opposite behavior in DMF as P-type switches (bistable system) were observed. The obtained results lead to a conclusion that by variation of the solvent environment a direct control over the bidirectional switching behaviour from T-type to P-type can be achieved.

 Received 1st July 2020,
 Accepted 31st July 2020

DOI: 10.1039/d0nj03301d

rsc.li/njc

1. Introduction

The control of molecules by direct contact with light as photochromic compounds attracts much attention due to the chromogenic properties associated with their bistability (on/off). These promising compounds, possessing photoswitchable properties under an external stimulus and leading to reversible structural changes occurring by the isomerization of the photosensitive units, are of the utmost importance when it comes to embedding such entities for molecular electronics and biomedical applications.¹ A light-induced isomerization process is usually accompanied by a number of changes in molecular geometry, crystal shape, conductance, polarity, *etc.*^{2–5} Photochemical conversion is based on photoisomerization or photo-rearrangement of the electrons of frontier molecular orbitals, which are involved in the electron transition from the ground to

the excited state of the molecules. This action could be included in many other processes such as photosynthesis, activation of specialized receptors in living organisms, and photodynamic therapy, and in optical sensors, photoswitches, solar cells, and so on.^{6–13}

The chemistry of the imine or azomethine group ($\geq\text{C}=\text{N}-$) plays a vital role in the progress of chemical science.¹⁴ The compounds of this group are known as Schiff bases, which are usually synthesized from the condensation of primary amines and compounds having active carbonyl groups. Schiff bases derived from aromatic amines and aromatic aldehydes have a wide variety of applications such as in biological and catalytic applications. They are also used as ligands to obtain metal complexes with different metal ions in coordination chemistry, biochemistry, supramolecular chemistry, materials science, separation and encapsulation processes, and formation of compounds with unusual properties and structures. Schiff base compounds containing some pharmacophore groups as well as their complexes with monovalent and bivalent metal ions have attracted significant attention.^{15–17} Particular attention has been paid to the imine \rightarrow enamine tautomeric form and epimerization of the Schiff bases of gossypol.¹⁸ Furthermore, Schiff bases represent an important class of organic compounds, especially in the medicinal and pharmaceutical fields. Several Schiff bases have been reported for their significant biological activities like antitumor,¹⁹ anti-inflammatory,²⁰ antimicrobial,²¹ and anticonvulsant activities.²² For example, Isatin ligands have been reported to exhibit anticonvulsant

^a Department of Organic Chemistry, University of Chemical Technology and Metallurgy, 1756 Sofia, Bulgaria. E-mail: pepi_37@abv.bg

^b Department of Analytical Chemistry, University of Chemical Technology and Metallurgy, 1756 Sofia, Bulgaria

^c Institute of Mineralogy and Crystallography, Bulgarian Academy of Sciences, Sofia 1113, Bulgaria

^d Department of Optical Metrology and Holography, Institute of Optical Materials and Technologies, Bulgarian Academy of Science, 1113 Sofia, Bulgaria.

E-mail: antonchem@abv.bg

† Electronic supplementary information (ESI) available. CCDC 2011731–2011733. For ESI and crystallographic data in CIF or other electronic format see DOI: 10.1039/d0nj03301d

activity and may be included in antiepileptic drugs.²³ In the case of these compounds, it has been suggested that the azomethine linkage might be responsible for their biological activities.²⁴ Among the other applications, they are used in optical computers, to measure and control the intensity of the radiation, molecular memory storage, as organic materials in reversible optical memories, and biological systems as photo-detectors.^{25,26} Due to their photochromic properties, Schiff bases could behave as photostabilizers, dyes for solar cells (collectors) and solar filters.²⁷ It should be noted that they possess very interesting properties namely optical nonlinearity and the ability to create the structure for a new type of molecular conductor using electrical properties for proton transfer.^{28,29}

Hydantoin derivatives are an important class of pharmaceutical compounds, and their synthesis has received considerable attention in organic chemistry, materials science and medicinal chemistry.^{30–32} The need(s) to design, synthesize and produce novel structures makes them important in terms of novel drug development and for understanding the structure–activity relationship.³³ The azomethine group ($-\text{CH}=\text{N}-$) is structurally similar to the azobenzene group possessing alike switchable groups ($-\text{N}=\text{N}-$, $>\text{C}=\text{C}\leq$) that can be involved in the photoisomerization $E/Z/E$ cycle. Nowadays, photoisomerization processes are extensively used in everyday life and in practice. Most of the studies on their photochromism have been performed with benzylidene aniline-type azomethines.^{40–42} The thermodynamically more stable E isomer is non-planar with a dihedral angle between the planes of aromatic rings varying around $\sim 41\text{--}55^\circ$.⁴¹ On the other hand, the lower activation energy barrier of the thermal Z/E isomerization of azomethine compounds is advantageous, and allows for rapid reversible geometrical changes in light-driven molecular devices.⁴¹ There are many studies on photochemistry and applications of azomethines as photonic compounds, but there is little information on the photoisomerization properties of biologically active azomethines.^{43–45}

We have recently reported the synthesis, characterization and biological activity of different hydantoin derivatives.^{34–39,49} Furthermore, in our previous studies, we have investigated several E/Z photoswitching behaviours of 5,5'-substituted hydantoin Schiff base derivatives with different electron-donor and electron-acceptor groups.^{39,49} This work is a continuation of our studies on the synthesis and characterization of novel hydantoin Schiff bases. Bearing in mind the promising properties, we were motivated to carry out the synthesis and characterization by single crystal X-ray structures and electrochemistry of some 3-amino-5,5'-dimethylhydantoin Schiff bases containing different aromatic moieties. The photoswitching $E/Z/E$ and enol/keto/enol behaviors (so called bidirectional switching) were studied under long wavelength UV-light at 350 nm in nonpolar 1,4-DOX and polar aprotic DMF. The aim was to investigate the kinetics of solvent-driven photo-conversion in terms of the structure–property relationship. This was achieved by a combined approach using optical (absorbance and emission) spectroscopy and ground state and excited state DFT calculations. The obtained information could be useful for the design of new photoswitching systems with various photochemical and biological properties.

2. Experimental section

2.1. Synthesis

All reagents and solvents were of analytical or HPLC grade and were bought from Fluka or Merck, and used without further purification. Melting points (m.p.) were determined on a Koffler microscope and were uncorrected. The reactions were controlled by TLC on pre-coated plates of Silica gel 60 F254 (Merck) with a 3:2 mixture of methanol and ethyl acetate used as the mobile phase. Spots on TLC chromatograms were detected by chlorine/ o -toluidine reactions. The 3-amino-5,5'-diphenylimidazolidine-2,4-dione (**2**) was synthesized from 5,5'-diphenylimidazolidine-2,4-dione (**1**) by means of $\text{NH}_2\text{NH}_2\cdot\text{H}_2\text{O}$ according to our previous work.³⁴

2.1.1. General procedure for the preparation of new 3-amino-5,5'-diphenylhydantoin Schiff bases (SB1–SB4). 3-amino-5,5'-diphenylhydantoin (1.0 equiv.) and the corresponding aromatic aldehydes (1.0 equiv.) were suspended in anhydrous methanol (20 mL). Subsequently, a catalytic amount of glacial acetic acid was added (3–4 drops) and the mixture was heated to reflux for about 4 h without stirring until all starting materials dissolved. The product precipitates from the solution upon cooling to room temperature and was filtered off to yield the pure desired Schiff bases. The crude material was recrystallized from methanol.

(*E*)-5,5'-Diphenyl-3-((thiophen-2-ylmethylene)amino)imidazolidine-2,4-dione (SB1). Yield: 1.23 g (91%). M.p. 182–183 °C. Rf = 0.90. ATR-IR (cm^{-1}): 3194 ($\nu_{\text{C-H}}-\text{CH}=\text{N}-$), 1766 ($\nu_{\text{s}}\text{C}=\text{O}$ imide), 1712 ($\nu_{\text{as}}\text{C}=\text{O}$ imide), 1587 ($\nu_{\text{C=N}}-\text{CH}=\text{N}-$), 1315 and 1241 (C–N), 721 ($\rho_{\text{C=N}}$). ¹H NMR (600 MHz, DMSO- d_6), δ (ppm): 9.41 (d, $J = 1.0$ Hz, 1H), 7.85 (dt, $J = 5.0, 1.1$ Hz, 1H), 7.70 (dd, $J = 3.8, 1.2$ Hz, 1H), 7.47–7.32 (m, 10H), 7.21 (dd, $J = 5.0, 3.7$ Hz, 1H). ¹³C NMR (151 MHz, DMSO- d_6), δ (ppm): 169.59, 155.89, 152.84, 139.63, 137.91, 135.33, 132.28, 129.16, 128.91, 128.80, 127.28, 67.98, 40.48. HRMS (ESI) calculated for $\text{C}_{20}\text{H}_{15}\text{N}_3\text{O}_2\text{S}$, [MH^+]: 362.0885; found: 362.0965.

(*E*)-3-((2-Hydroxybenzylidene)amino)-5,5'-diphenylimidazolidine-2,4-dione (SB2). Yield: 1.23 g (89%). M.p. 221–222 °C. Rf = 0.85. ATR-IR (cm^{-1}): 3385 (ν_{OH}), 3173 ($\nu_{\text{C-H}}-\text{CH}=\text{N}-$), 1774 ($\nu_{\text{s}}\text{C}=\text{O}$ imide), 1720 ($\nu_{\text{as}}\text{C}=\text{O}$ imide), 1618 and 1600 ($\nu_{\text{C=N}}-\text{CH}=\text{N}-$), 1258 (C–N), 745 ($\rho_{\text{C=N}}$). ¹H NMR (600 MHz, DMSO- d_6), δ (ppm): 10.59 (s, 1H), 10.09 (s, 1H), 9.49 (s, 1H), 7.75 (dd, $J = 7.8, 1.7$ Hz, 1H), 7.48–7.43 (m, 5H), 7.43–7.33 (m, 8H). ¹³C NMR (151 MHz, DMSO- d_6), δ (ppm): 169.66, 158.52, 158.45, 152.82, 139.62, 133.95, 129.17, 128.99, 128.91, 128.56, 127.29, 120.04, 119.04, 117.07, 67.97. HRMS (ESI) calculated for $\text{C}_{22}\text{H}_{17}\text{N}_3\text{O}_3$, [MH^+]: 372.1270; found: 372.1462.

(*E*)-3-((4-Nitrobenzylidene)amino)-5,5'-diphenylimidazolidine-2,4-dione (SB3). Yield: 1.27 g (85%). M.p. 209–210 °C. Rf = 0.86. ATR-IR (cm^{-1}): 3116 ($\nu_{\text{C-H}}-\text{CH}=\text{N}-$), 1781 ($\nu_{\text{s}}\text{C}=\text{O}$ imide), 1724 ($\nu_{\text{as}}\text{C}=\text{O}$ imide), 1517 ($\nu_{\text{C=N}}-\text{CH}=\text{N}-$), 1338 (ν_{NO_2}), 1217 (C–N), 730 ($\rho_{\text{C=N}}$). ¹H NMR (600 MHz, DMSO- d_6), δ (ppm): 10.19 (s, 1H), 9.54 (s, 1H), 8.37–8.31 (m, 2H), 8.13–8.08 (m, 2H), 7.48–7.37 (m, 10H). ¹³C NMR (151 MHz, DMSO- d_6), δ (ppm): 169.75, 157.22, 152.56, 149.48, 139.66, 139.49, 129.59, 129.21, 128.99, 127.30, 124.62, 67.96. HRMS (ESI) calculated for $\text{C}_{22}\text{H}_{16}\text{N}_4\text{O}_4$, [MH^+]: 401.1172; found: 401.1375.

Table 1 Crystal data and structure refinement parameters for SB2, SB3 and SB4

Compound	SB2	SB3	SB4
Empirical formula	C ₂₂ H ₁₇ N ₃ O ₃	C ₂₂ H ₁₆ N ₄ O ₄	C ₂₁ H ₁₆ N ₄ O ₂
Formula weight	371.38	400.39	356.38
Temperature/K	290	290	290
Crystal system	Triclinic	Monoclinic	Monoclinic
Space group	<i>P</i> 1̄	<i>P</i> 2 ₁ / <i>c</i>	<i>I</i> 2/ <i>a</i>
<i>a</i> /Å	8.5374(8)	9.5170(5)	16.3125(6)
<i>b</i> /Å	10.4625(17)	10.8616(7)	8.4276(3)
<i>c</i> /Å	11.6521(17)	18.5972(10)	27.2914(10)
α /°	107.718(14)	90	90
β /°	96.228(10)	100.902(5)	105.355(4)
γ /°	106.521(11)	90	90
Volume/Å ³	928.6(2)	1887.70(19)	3618.0(2)
<i>Z</i>	2	4	8
$\rho_{\text{calc}}/\text{g cm}^{-3}$	1.328	1.409	1.309
μ/mm^{-1}	0.090	0.100	0.087
<i>F</i> (000)	388.0	832.0	1488.0
Crystal size mm ⁻³	0.2 × 0.15 × 0.15	0.3 × 0.2 × 0.2	0.2 × 0.2 × 0.2
Radiation	Mo K α (λ = 0.71073)	MoK α (λ = 0.71073)	MoK α (λ = 0.71073)
2 θ range for data collection/°	5.474 to 57.12	5.618 to 56.8	5.952 to 56.942
Index ranges	-11 ≤ <i>h</i> ≤ 11, -10 ≤ <i>k</i> ≤ 13, -15 ≤ <i>l</i> ≤ 12	-10 ≤ <i>h</i> ≤ 12, -9 ≤ <i>k</i> ≤ 12, -23 ≤ <i>l</i> ≤ 24	-20 ≤ <i>h</i> ≤ 21, -8 ≤ <i>k</i> ≤ 11, -34 ≤ <i>l</i> ≤ 35
Reflections collected	5865	11 248	12 845
Independent reflections	5865 [<i>R</i> _{int} = 0.0455, <i>R</i> _{sigma} = 0.0886]	4009 [<i>R</i> _{int} = 0.0291, <i>R</i> _{sigma} = 0.0311]	3912 [<i>R</i> _{int} = 0.0317, <i>R</i> _{sigma} = 0.0307]
Data/restraints/parameters	5865/1/262	4009/0/275	3912/0/248
Goodness-of-fit on <i>F</i> ²	1.024	1.043	1.077
Final <i>R</i> indexes [<i>I</i> ≥ 2 σ (<i>I</i>)]	<i>R</i> ₁ = 0.0618, <i>wR</i> ₂ = 0.1746	<i>R</i> ₁ = 0.0471, <i>wR</i> ₂ = 0.1112	<i>R</i> ₁ = 0.0482, <i>wR</i> ₂ = 0.1154
Final <i>R</i> indexes [all data]	<i>R</i> ₁ = 0.1352, <i>wR</i> ₂ = 0.1927	<i>R</i> ₁ = 0.0713, <i>wR</i> ₂ = 0.1250	<i>R</i> ₁ = 0.0764, <i>wR</i> ₂ = 0.1320
Largest diff. peak/hole/e Å ⁻³	0.18/-0.23	0.14/-0.20	0.15/-0.17

(*E*)-5,5'-Diphenyl-3-((pyridin-2-ylmethylene)amino)imidazolidine-2,4-dione (SB4). Yield: 1.17 g (88%). M.p. 215–216 °C. *R*_f = 0.89. ATR-IR (cm⁻¹): 3004 ($\nu_{\text{C-H}}$ -CH=N-), 1781 (ν_{s} C=O imide), 1727 (ν_{as} C=O imide), 1586 and 1569 ($\nu_{\text{C=N}}$ -CH=N-), 1343 (C-N), 718 ($\rho_{\text{C=N}}$). ¹H NMR (600 MHz, DMSO-*d*₆), δ (ppm): 10.15 (s, 1H), 9.39 (s, 1H), 8.70 (ddt, *J* = 4.9, 1.8, 0.9 Hz, 1H), 8.04 (dt, *J* = 8.0, 1.1 Hz, 1H), 7.95 (td, *J* = 7.7, 1.7 Hz, 1H), 7.52 (ddt, *J* = 7.0, 4.9, 1.0 Hz, 1H), 7.48–7.33 (m, 10H). ¹³C NMR (151 MHz, DMSO-*d*₆), δ (ppm): 169.87, 158.88, 152.67, 152.55, 150.43, 139.54, 137.72, 129.19, 128.96, 127.32, 126.33, 121.30, 67.89. HRMS (ESI) calculated for C₂₁H₁₆N₄O₂, [MH⁺]: 357.1273; found: 357.1477.

2.2. Single crystal structure analysis

A suitable single crystal of compounds SB2, SB3 and SB4 was mounted on a glass capillary. All intensity and diffraction data were collected on a Agilent SupernovaDual diffractometer equipped with an Atlas CCD detector using micro-focus Mo K α radiation (λ = 0.71073 Å) at 290 K. The crystal structures were solved by direct methods with ShelxS and refined with the full-matrix least-squares method of *F*² with ShelXL programs.⁵⁰ All non-hydrogen atoms were located successfully from Fourier maps and were refined anisotropically. Hydrogen atoms for N and O were located from difference Fourier maps and refined isotropically while all other hydrogen atoms were placed at calculated positions using a riding scheme (*U*_{eq} = 1.2 for C-H = 0.93 Å). The most important crystallographic parameters such as bond lengths, angles and torsion angles are shown in Tables 1, 3 and Table S1 (ESI[†]). The ORTEP View⁵¹ of the molecules present in the asymmetric unit (ASU) with the atomic displacement parameter (ADP) at 50% is shown in Fig. 1. Crystallographic data

have been deposited in the Cambridge Crystallographic Data Center as supplementary publication number CCDC 2011731, 2011732 and 2011733 (and ESI[†]) for SB2, SB3 and SB4, respectively. All of the graphics were created using ORTEP or MERCURY⁵² programs.

2.3. Physical measurements

2.3.1. Spectral measurements. The NMR spectra were recorded on a Bruker Avance II+ spectrometer operating with frequency 600 MHz for ¹H and 125 MHz for ¹³C in DMSO-*d*₆. (Fig. S1–S8, ESI[†]). Chemical shifts δ are reported in ppm, and coupling constants *J* are reported in Hz. ATR-IR spectra of the compounds were recorded on a Bruker Tensor 27 FTIR spectrophotometer in the range of 4400–600 cm⁻¹ with a resolution of 2 cm⁻¹ at room temperature. The external reflection diamond crystal has been used and the samples were scanned 128 times. The molecular mass and purity of the compounds were confirmed by high-resolution electrospray mass spectrometry on a Q Exactive hybrid quadrupole Orbitrap mass spectrometer (ThermoScientific) equipped with a heated electrospray ionization module IonMax (ThermoScientific). The UV-VIS spectra were recorded on a Cary 5E-UV-VIS-NIR spectrophotometer. The steady-state fluorescence spectra were recorded *via* a FluoroLog 3-22 (HORIBA) spectrofluorometer in the range of 200–800 nm with a resolution of 0.5 nm and double-grating monochromators by excitation wavelength set near to the absorption maxima of the SBs. The concentration of the compounds was *C*_M = ~4 × 10⁻⁵ mol L⁻¹.

2.3.2. Photoisomerization experiments. The photoinduced *E/Z* photoisomerization and enol/keto tautomerization experiments

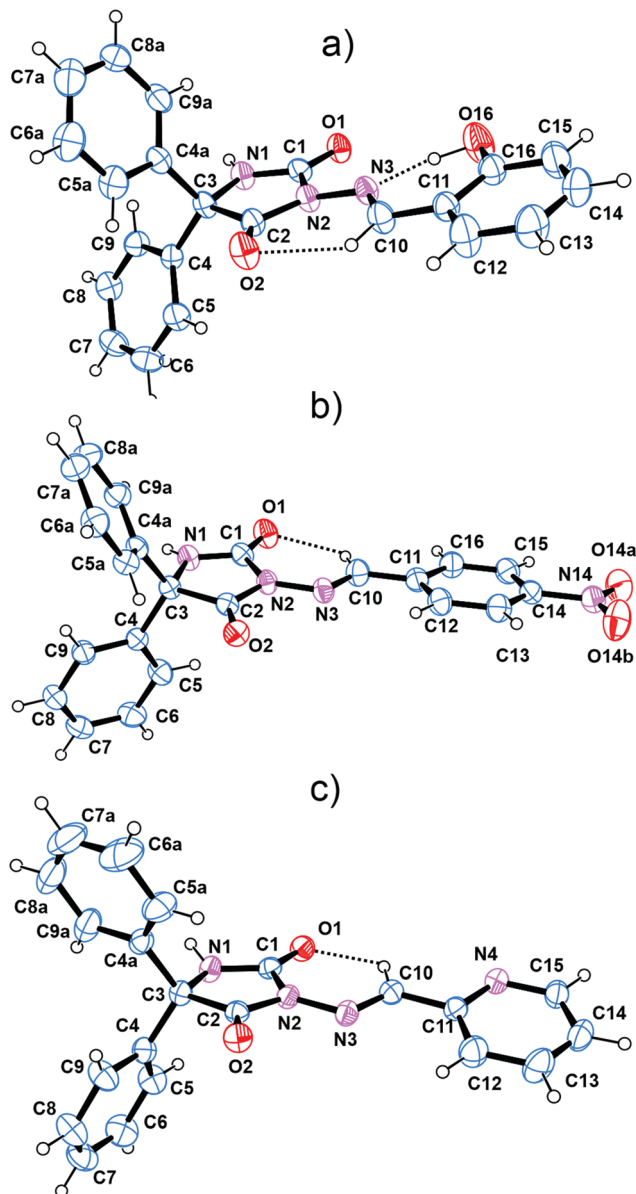


Fig. 1 Ortep view and numbering scheme of the asymmetric structure of compounds (a) **SB2** (b) **SB3** and (c) **SB4**; ADP is at the 50% level, hydrogen atoms are shown as spheres with arbitrary radii. Intramolecular hydrogen bonding ($O_{16}-H_{16}\cdots N_3$) and weak interactions ($C_{10}-H_{10}\cdots O_1$ and $C_{10}-H_{10}\cdots O_2$) are shown as dotted lines.

were performed in 1,4-DOX (1,4-dioxane) and DMF (dimethylformamide) solutions at room temperature on a custom-built optical set-up with a high resolution HR4000 spectrometer (Ocean Optics) operating in the range of 200–1000 nm. As the light source was used, a pulsed xenon light source (PX-2) was directed to pass through the dye solutions and to get directly to the spectrometer through optical output fiber. Special care has been taken to eliminate all possible sources of stray light. The source of long wavelength UV irradiation was a broadband lamp at $\lambda_{\max} = 350$ nm (output power 10 W), perpendicularly directed to the probe beam. The illumination time was set at 600 s until the photostationary state (PSS) was reached. After exposure, the

probes underwent *Z/E* (**SB1**, **SB3**, and **SB4**) and keto/enol (**SB2**) relaxation in darkness for 600 s and 60 min at room temperature. The spectra were collected every 2 s during the entire experiment with the integration time being set at 100 ms and scans to average at 10. Before the experiments start, the solutions of the SBs were stored in the dark overnight. The concentrations were $C_M = \sim 4 \times 10^{-5}$ mol L⁻¹ and $C_M = \sim 1 \times 10^{-6}$ mol L⁻¹ for **SB4** in 1,4-DOX.

2.3.3. DFT quantum chemical calculations. The molecular geometry and electronic structure optimization of the studied SBs were performed using GAUSSIAN 09W software package using density-functional theory DFT/B3LYP exchange–correlation hybrid functional combined with the standard 6-311+G(2d,p) basis set both *in vacuo* and in DMF and 1,4-DOX.⁵³ The interactions between the molecule and the solvent were evaluated at the same basis set by a polarizable continuum model using the integral equation formalism variant (IEFPCM). TD-DFT calculations were performed after optimization of geometry in *E/Z* isomers and enol/keto tautomers of the compounds at the same basis set using DMF and 1,4-DOX solvents. The frequency analysis was performed at the same level of theory to characterize the stationary points on the potential surface and no imaginary frequencies were found.

2.3.4. Kinetics data. The degrees of *E* → *Z* photoisomerization and photoinduced enol → keto tautomerization as well as *R* at the PSS, were determined according to eqn (1) and the rate constant *k* was fitted by eqn (2) (*E* → *Z* and enol → keto) and eqn (3) (*Z* → *E* and keto → enol) taking into account first-order of the reactions:^{54–59}

$$R = \frac{A_0 - A_\infty}{A_0} \times 100. \quad (1)$$

$$\ln\left(\frac{A_0 - A_\infty}{A_t - A_\infty}\right) = k \cdot t. \quad (2)$$

$$\ln\left(\frac{A_\infty - A_0}{A_\infty - A_t}\right) = k \cdot t. \quad (3)$$

where A_0 is the initial absorbance, A_t is the absorbance at the moment *t* during the irradiation and A_∞ represents the absorbance at the PSS.

2.3.5. Description of the efficiency of enol → keto conversion in the excited state (η_T). For qualitative evaluation of the proton transfer in the excited state, we have used a previously described method by L. Antonov and co-workers, where the assumption is that in the excited state enol form undergoes fast transformation to the excited keto and the resulting emission is characterized by large Stokes shifts compared to the enol one.⁶⁰ The authors have estimated the relative fraction of the enol form using the excitation spectrum, which is converted into the keto form through ESIPT. They express the contributions of both forms by the following equations (eqn (4) and (5)).⁵⁴

$$I_{\text{exc}}(E) = A_E \times Q_K \times \left(\frac{k_{PT}}{k_{PT} + k_d(E)}\right). \quad (4)$$

$$I_{\text{exc}}(K) = A_K \times Q_K \quad (5)$$

where A_E and A_K are the absorbance maxima of the enol and keto forms; $I_{\text{exc}}(E)$ and $I_{\text{exc}}(K)$ are the excitation intensities at the same wavelengths; k_{PT} is the ESIPT rate, $k_d(E)$ is the decay rate and Q_K is the quantum yield of the keto form. If the $k_{\text{PT}}/k_{\text{PT}} + k_d(E)$ is defined as the efficiency of conversion of enol into keto form η_T , from eqn (4) and (5), we can use the following expression (eqn (6)):

$$\eta_T = \frac{I_{\text{exc}}(E) \times A_K}{I_{\text{exc}}(K) \times A_E} \times 100. \quad (6)$$

2.3.6. Electrochemistry. For the electrochemical analysis, a computerized voltammetric technique Metrohm 797 VA trace analyser and a 797 VA stand with experimental control and data acquisition were used. A voltammetric cell system consisted of three electrodes was constructed with a saturated Ag/AgCl reference electrode, a platinum auxiliary electrode and a hanging mercury drop electrode (HMDE of 0.015 cm² drop area) as the working electrode area.

For the electrochemical experiments, compounds were dissolved in DMSO and the concentrations of stock solutions were as follows: 4.46×10^{-3} **SB1**; 3.08×10^{-3} **SB2**; 3.18×10^{-3} **SB3**; 3.51×10^{-3} **SB4** mol L⁻¹. Electrolyte medium (7 mL) from DMF, CH₃OH (with 0.04 mol L⁻¹ tetrabutyl ammonium perchlorate, TBAP) and LiOH (0.01622 mol L⁻¹): LiCl (0.01 mol L⁻¹) (LiOH/LiCl, pH 12.21) were used. The analysed stock solutions were exposed to *E/Z* isomerization by the UV irradiation at $\lambda = 350$ nm for 600 s. The voltamperograms of irradiated compounds were immediately recorded under the same supporting electrolyte and conditions. Prior to each experiment, the working solution was purged with high purity argon, and an argon atmosphere was maintained throughout the experiment. All used reagents were of analytical grade.

2.3.7. Coulometry measurements (controlled potential electro-lysis). Controlled potential coulometric (CPC) experiments were performed with the electrolysis cell designed similar to that described previously.⁶¹ A coulometric cell of a three-electrode configuration *viz.* a mercury pool cathode, a platinum wire counter electrode (separated from the main solution by a glass frit) and a saturating calomel electrode (SCE) as a reference electrode was used. An indicator current of the supporting electrolyte was measured with a microammeter in the range of 15 pA after bubbling the solution with pure nitrogen gas for about 10–15 minutes. The depolarizer solution containing compounds was introduced into the cell at a constant value of the background current. The selected potential was adjusted to be equal to the polarographic peak potential plus 0.1 volt or at the beginning of the limiting current of the polarographic peak. The accumulated charge (Q in coulombs) is read directly from a digital coulometer (Table 2).

3. Results and discussion

3.1. Synthesis and crystal structure

Four novel 3-amino-5,5'-diphenylhydantoin Schiff Bases (**SB1–SB4**) were synthesized and spectrally characterized for their photo-physical properties as photoswitches. For their preparation, first

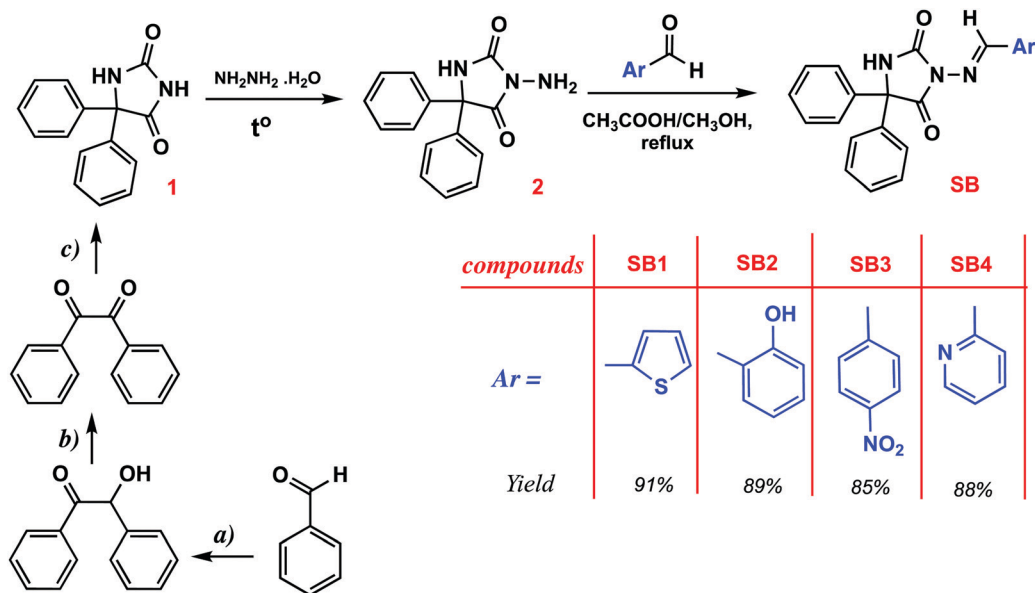
Table 2 Controlled potential electrolysis (coulometry) of SBs (**1–4**) before and after UV illumination with $\lambda = 350$ nm at pH 12.21 (LiOH/LiCl) and applied potential: -1.60 V

Compounds	Mol. wt	Weight of the sample, (g) $\times 10^{-3}$	Number of coulombs	Total number of electrons
SB1	361.42	1.25	0.617	$1.85 \approx 2$
SB2	371.39	1.15	0.601	$2.01 \approx 2$
SB3	400.39	1.37	0.716	$2.17 \approx 2$
SB4	356.38	1.18	0.654	$2.05 \approx 2$

5,5'-diphenylimidazolidine-2,4-dione needs to be synthesized, and second 3-amino-5,5'-diphenylimidazolidine-2,4-dione has to be obtained. Unfortunately, only a few protocols for obtaining 5,5'-diphenylimidazolidine-2,4-dione have been reported.^{46–48}

As a potential skeleton/fragment for pharmaceutical and many other research and development applications, finding a general and improved method to synthesize 5,5'-diphenylimidazolidine-2,4-dione analogues is essential. The starting compound 5,5'-diphenylimidazolidine-2,4-dione (5,5'-diphenylhydantoin is also known as Phenytoin) used to obtain the desired SBs was synthesized from benzaldehyde under the influence of potassium cyanide in aqueous alcohol and underwent a dimolecular condensation reaction and gave benzoin (see Scheme 1a). After that, the oxidation of benzoin with FeCl₃·6H₂O yielded benzil (Scheme 1b). Then the benzil on treatment with urea in alcoholic solution in the presence of KOH (30%) first gave benzilic acid, then through a condensation reaction with urea and after acidification of the filtrate with 6 M sulfuric acid gave 5,5'-diphenylhydantoin (**1**) (Scheme 1c). 3-amino-5,5'-diphenylhydantoin (**2**) was successfully obtained by the reaction of (**1**) and hydrazine hydrate following our previous work.³⁴ The studied **SB1–SB4** were synthesized by a condensation reaction between (**2**) and the corresponding aromatic aldehyde in an equimolar ratio in absolute methanol in the presence of catalytic amounts of glacial acetic acid (Scheme 1). **SB1** and **SB4** were designed with a donor thiophene/pyridine ring, while **SB3** was designed with an acceptor 4-nitrophenyl moiety. The structure of **SB2** contains the salicylic part and is able to form six-membered intramolecular hydrogen bonding between the phenol –OH group and nonbonding electron pairs of azomethine nitrogen. The structure of the obtained compounds was determined by ATR-IR, NMR (¹H and ¹³C) and HRMS (ESI⁺) methods. The ¹H-NMR spectra of the SBs are characterized by singlet of the azomethine proton (CH=N) at: 9.41 ppm for **SB1**; 10.59 ppm for **SB2**; 10.19 ppm for **SB3**; 10.15 ppm for **SB4**. The chemical shifts in the ¹³C-NMR spectra are between 152 and 158 ppm, which represent a singlet, characteristic of the carbon atom of the azomethine group. The ATR-IR spectra also confirm the structure of the above-mentioned compounds, where the characteristic bands are attributed to the –CH=N– ($\nu_{\text{C-H}}$ 3194–3097 cm⁻¹), –CH=N– ($\nu_{\text{C=N}}$ 1630–1600 cm⁻¹), –C=N– ($\delta_{\text{C-N}}$ 1366–1244 cm⁻¹), and –C=N– ($\rho_{\text{C=N}}$ 728–722 cm⁻¹) vibrations that are used in the structural characterization of this type of compound.

Single crystals of **SB2**, **SB3** and **SB4** suitable for X-ray diffraction analysis were obtained by slow evaporation from methanol, ethanol and methanol:ethanol (3:1) solutions of



Scheme 1 Synthetic pathway of the 3-amino-5,5'-diphenylhydantoin Schiff bases (**SB1**, **SB2**, **SB3** and **SB4**): (a) KCN/EtOH, reflux; (b) FeCl₃·6H₂O, reflux; (c) NH₂CONH₂/EtOH and KOH (30%), 6 M H₂SO₄.

respective compounds. The 2-hydroxybenzylidene derivative (**SB2**) crystallizes in the triclinic space group $P\bar{1}$ with one molecule in the asymmetric unit, while the 4-nitrobenzylidene (**SB3**) and pyridin-2-ylmethylene (**SB4**) derivatives crystallize in the monoclinic space group $P2_1/c$ and $I2/a$, both with one molecule in the asymmetric unit. The corresponding Ortep drawings of the molecules present in the asymmetric and crystallographic and structural data are summarized in Fig. 1 and Table 1. As shown in Fig. 2, the single crystal X-ray diffraction analysis results reveal that in the solid crystalline state the *E*-isomers of this series of compounds are obtained. The 5,5'-diphenylimidazolidine-2,4-dione moiety disclose a highly conserved molecular geometry (Table S1, ESI[†]) even though the rotation of the two phenyl rings along C₃-C₄ and C₃-C_{4A} bonds is not hampered. The 2-hydroxybenzylidene, 4-nitrobenzylidene and pyridin-2-ylmethylene substituents are linked to the phenytoin through N=C (N₃-C₁₀) and C-C (C₁₀-C₁₁) bonds with lengths as short as 1.263(2) and 1.444(5) Å, respectively, confirming the conjugated electronic nature of the molecules. The N-N, N=C and C-C sequences of bonds between the hydantoin and the substituents result in a meandering and elongated, almost planar molecular structure. Indeed, only a very small average deviation from the mean plane of the N₂-N₃-C₁₀-C₁₁

is detected (max rmsd of 0.013 Å for **SB2**). The aromatic ring systems in **SB2-4** (with the exception of the two phenyls linked to the spiro center) are also positioned in the N₂-N₃-C₁₀-C₁₁ plane (the angle with the hydantoin plane is 12.207, 3.503, 11.766° in **SB2-4**, respectively, the angle with phenol is 2.939°, with nitrobenzene 6.114°, with pyridine 3.945°, between hydantoin and phenol mean planes 11.808° in **SB2**, hydantoin/nitrobenzene 9.460° in **SB3**, and hydantoin/pyridine 15.659° in **SB4**). The planarity is further strengthened by weak intramolecular C-H···O interactions (Table 3 and Fig. 1). The crystal structure of **SB2** discloses also a second intramolecular hydrogen bonding interaction O₁₆-H₁₆···N₃. Although this hydrogen bonding interaction is just slightly (energetically) more favorable than the C-H···O interaction, the last one is achieved with O1 for **SB2** while in **SB3** and **SB4** the interaction is C₁₀-H₁₀···O₂. This results in a change of the C₁-N₂-N₃ angle from ~130° in **SB3** and **SB4** to ~117° in **SB2**. In addition to the intramolecular interactions, intermolecular hydrogen bonding interactions, typical for hydantoin, are present (Fig. 3 and Table 3). In **SB2** adjacent molecules produce a dimer with the R₂²(8) graph set while infinite chains are produced in **SB3** and **SB4**. In the presence of several aromatic ring systems, one could hypothesize that the three-dimensional arrangement of the molecules in the crystal

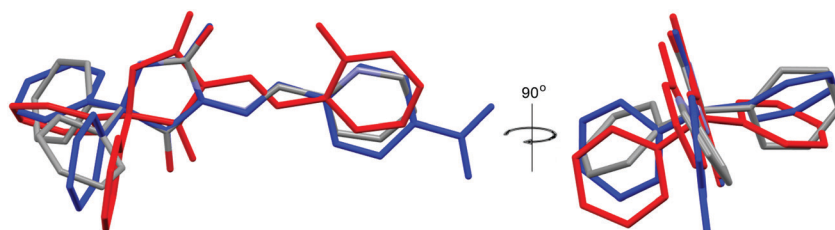


Fig. 2 Representation of the overlay of the molecules of **SB2** (in red), **SB3** (in blue) and **SB4** disclosing the subtle differences in the molecular structure.

Table 3 Hydrogen bonds for **SB2**, **SB3** and **SB4**

D	H	A	$d(\text{D-H})/\text{\AA}$	$d(\text{H-A})/\text{\AA}$	$d(\text{D-A})/\text{\AA}$	$\text{D-H-A}/^\circ$
SB2						
C ₁₀	H ₁₀	O ₂	0.93	2.28	2.917(5)	125.5
N ₁	H ₁	O ₁ ¹	0.92(4)	1.94(4)	2.847(4)	170(3)
O ₁₆	H ₁₆	N ₃	1.010(3)	1.65(3)	2.603(4)	155(6)
SB3						
C ₁₀	H ₁₀	O ₁	0.93	2.17	2.851(3)	129.5
N ₁	H ₁	O ₂ ¹	0.83(2)	2.07(2)	2.886(2)	167(2)
SB4						
C ₁₀	H ₁₀	O ₁	0.93	2.17	2.854(2)	129.5
N ₁	H ₁	N ₁ ¹	0.93	2.51	3.377(3)	154.7

$$^1 1 - x, 1 - y, 1 - z; ^2 1 - x, 1/2 + y, 1/2 - z; ^3 1 - x, -1/2 + y, 1.5 - z.$$

will disclose $\pi \cdots \pi$ interactions. Although one may claim that $\pi \cdots \pi$ stacking is present if characteristic (not relaxed) criteria are employed, the crystal structures do not reveal such interactions. Thus the packing is governed by the hydrogen bonding and the "rotation" of the phenyls along C₃-C₄ and C₃-C_{4A} bonds.

3.2. DFT calculations

DFT calculations provide insight into the electronic structures of the compounds in order to understand their structure-property relationship. The data from X-ray analysis were helpful to find the structures with minimal energies of the studied SBs. They were optimized as *E* and *Z* isomers (**SB1**, **SB3** and **SB4**) and enol/keto tautomer for **SB2** *in vacuo* and using solvation in DMF. The *E*-isomers in DMF is characterized by planar conformations with respect to the C₃₄-C₁₀-N₉-N₈ dihedral angle and nonplanar one by C₁₀-N₉-N₈-C₂ (Fig. 4 and Table 4). A comparative analysis of the geometry of *E*-isomers *in vacuo* with those in DMF displays planarization of the C₁₀-N₉-N₈-C₂ dihedral $\sim 4-5^\circ$. The observed DFT data *in vacuo* are supported by the current described X-ray analysis and our previous investigation of similar SBs containing 5,5'-dimethylhydantoin rings, the structures of which show a near planar conformation around the -CH=N- bond.³⁹ The same observation of DFT calculations has been made in our previous comparable study of the structural

effect of the 5,5'-dimethyl- and 5,5'-diphenylhydantoin SBs containing 2-hydroxy-1-naphthaldehyde and 1-naphthaldehyde moieties.⁴⁹ This allows us to make an indirect conclusion that 5,5'-disubstituted hydantoin do not influence the geometry of the -CH=N- bond. Due to the intramolecular six-membered hydrogen bonding, the 2-hydroxy substituted **SB2** is characterized by a planar structure both *in vacuo* and DMF. The reason for this difference is that the polar effect of proton acceptor aprotic DMF breaks down the weak six-membered H-bonding interactions of *E*-isomers between the azomethine H₁₁ atom and carbonyl oxygen of hydantoin. Such an effect in **SB2** is impossible because of the strong polar intramolecular H-bonding between *ortho* -OH and nonbonding electron pair of azomethine nitrogen.⁶² After photoisomerization to the more thermodynamically unstable *Z*-isomers, the C₃₄-C₁₀-N₉-N₈ dihedral angle reduces to the $4-7^\circ$ by twisting, while C₁₀-N₉-N₈-C₂ one varies from 60 to 80°, which is near to the T-shaped structure (Fig. 4 and Table 4). Such a structure suggests the formation of weak noncovalent interactions (NCIs) between aromatic H and nonbonding electron pairs of N(8) hydantoin with length $\sim 2.56-2.60 \text{ \AA}$, which is the main reason for relatively long thermal stability at room temperature (RT) as we consider in detail below in terms of the solvent dependence kinetics on bidirectional switching. Similar structures of azoheteroarenes with long thermal stability of *Z*-isomers have been studied by J. Calbo *et al.*⁶³ Based on DFT calculations and experimental kinetic data, the authors have concluded that T-shaped conformation *via* -N=N- bonds is preferable compared to the twisted one due to non-covalent interactions. The calculated ΔE values *in vacuo* are higher compared to the corresponding energies in DMF, especially for the **SB2** in enol/keto tautomerization (17.6 kcal mol⁻¹ *in vacuo* and 8.1 kcal mol⁻¹ in DMF), which is in agreement with the experimental results for the solvent effect on photoconversion, where in 1,4-DOX the photoinduced tautomerization does not proceed. Moreover, the keto tautomer in DMF shows a nonplanar relationship by C₁₀-N₉-N₈-C₂ dihedral $\sim 90^\circ$.

3.3. Photochromic and molecular switching behaviour

The kinetic analysis of *E/Z/E* photoisomerization (**SB1**, **SB3**, and **SB4**) and **SB2** enol/keto/enol phototautomerization cycles in

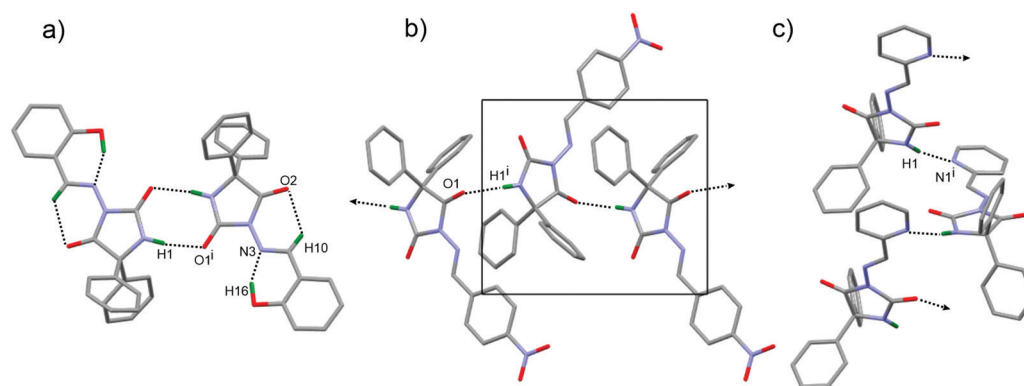


Fig. 3 Hydrogen bonding interactions in (a) **SB2**, (b) **SB3** and (c) **SB4**; symmetry codes (a) $-x, 1 - y, 1 - z$; (b) $1 - x, 1/2 + y, 1/2 - z$; and (c) $1 - x, -1/2 + y, 1.5 - z$.

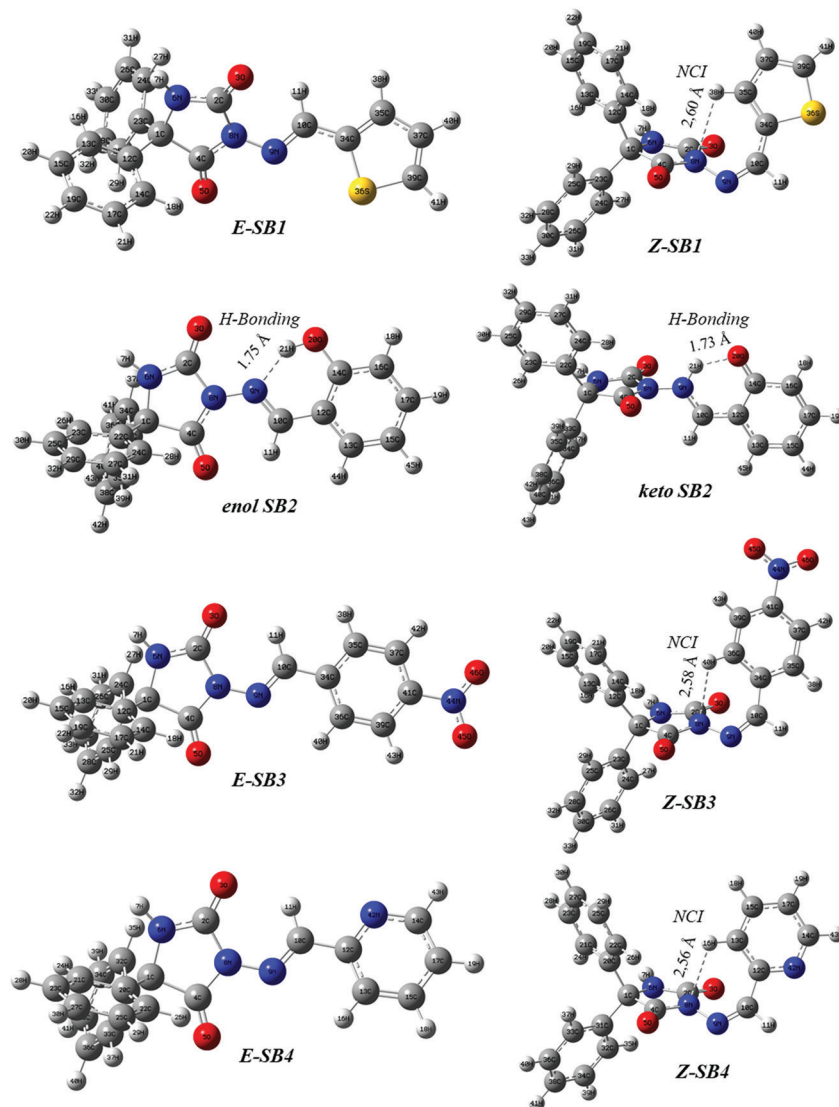


Fig. 4 Optimized molecular geometry of the SBs as *E*- and *Z*-isomers (**SB1**, **SB3**, and **SB4**) and enol/keto tautomers of **SB2** by DFT/B3LYP/6-311+G(2d,p) level of theory using IEFPCM in DMF.

Table 4 Theoretically calculated total electronic energy E (RB3LYP) and some dihedral angles (φ) of the studied SBs as *E*- and *Z*-isomers as well as enol/keto tautomers by DFT/B3LYP/6-311+G(2d,p) level of theory *in vacuo* and using IEFPCM in DMF

Compound	<i>Vacuo</i>				Solvation in DMF			
	$E(\text{RB3LYP})$ [kcal mol ⁻¹]	ΔE [kcal mol ⁻¹]	φ [°] C ₃₄ -C ₁₀ -N ₉ -N ₈	φ [°] C ₁₀ -N ₉ -N ₈ -C ₂	$E(\text{RB3LYP})$ [kcal mol ⁻¹]	ΔE [kcal mol ⁻¹]	φ [°] C ₃₄ -C ₁₀ -N ₉ -N ₈	φ [°] C ₁₀ -N ₉ -N ₈ -C ₂
<i>E</i> - SB1	-931463.7	8.3	-179.7	-5.3	-931474.4	6.3	178.1	-36.9
<i>Z</i> - SB1	-931455.4		5.9	75.5	-931468.1		4.5	-79.8
Enol SB2	-777407.1	17.6	179.8	4.5	-777417.4	8.1	179.9	0.04
Keto SB2	-777389.5		174.1	-16.2	-777409.3		-179	91.1
<i>E</i> - SB3	-858549.0	9.4	-179.7	-3.8	-858561.4	7.4	-179.9	10.1
<i>Z</i> - SB3	-858539.6		7.8	61.9	-858554.0		7.0	63.7
<i>E</i> - SB4	-740246.1	8.8	-179.5	-5.9	-740257.0	6.9	179.6	-21.4
<i>Z</i> - SB4	-740237.2		7.2	65.1	-740250.2		6.4	66.5

nonpolar aprotic 1,4-DOX and polar aprotic DMF allows understanding the behavior of the solvent environment on bidirectional photoswitching. The absorption changes in 1,4-DOX and DMF for *E/Z* isomerization indicate that the photostationary state (PSS) is

achieved up to 600 s (Fig. 5). Thermal *Z/E* relaxation at RT in 1,4-DOX becomes up to 600 s, while in DMF the *Z*-isomers at PSS are stable up to 60 min. The expected behavior of **SB2** based on ΔE DFT calculations displays that phototautomerization in

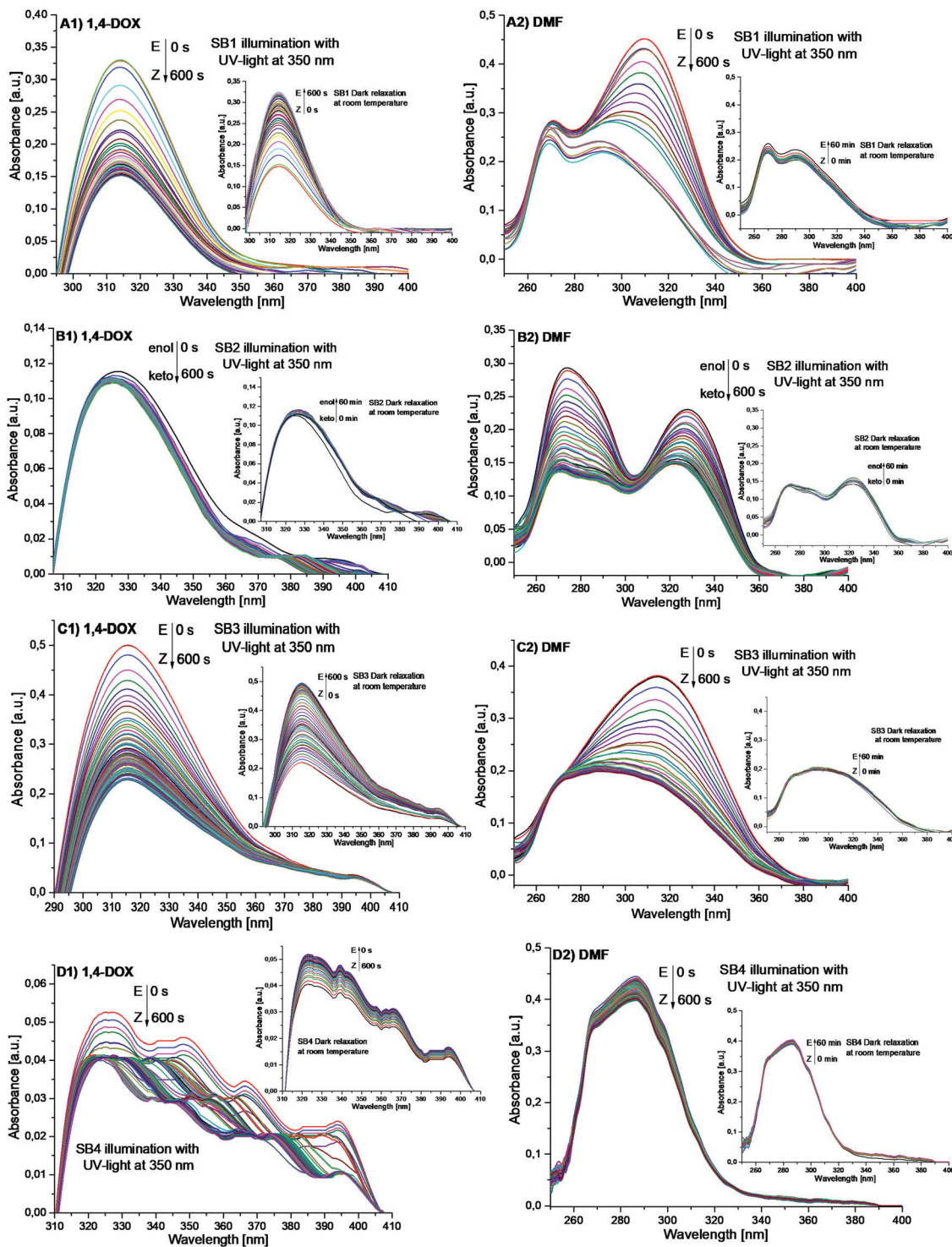


Fig. 5 Kinetics of the absorbance changes of *E/Z* isomerization (SB1, SB3 and SB4) and enol/keto tautomerization (SB3) in 1,4-DOX (A1, B1, C1, and D1) and DMF (A2, B2, C2, and D2) under long wavelength UV-light illumination at 350 nm. Inset graphics represent thermal relaxation in the dark in 1,4-DOX (up to 600 s) and DMF (up to 60 min) at room temperature.

nonpolar solvent does not proceed, while in polar one the PSS is achieved up to 600 s and the stability of the keto tautomer is up to 60 min (Fig. 5B1 and B2). The relatively long stability of the SBs in DMF is unusual because it is well known that the energy barrier of *Z/E* back relaxation of azomethines (70 kJ mol^{-1}) is

smaller than this of the azo compounds (95 kJ mol^{-1}).⁴¹ Taking into account first-order fitting of photoisomerization reactions, the degree of photoisomerization (*R*), rate constant (*k*) and half-life of reaction ($t_{1/2}$) were determined in both solvents (Table 5) (for more details see ESI†).^{64–68} The *R* and speed of *E/Z*

Table 5 Experimentally determined values of the photoisomerization degree (R), rate constants (k), the half-life of reaction ($t_{1/2}$) of E/Z photoisomerization and photoinduced enol/keto tautomerization as well as back Z/E and keto/enol relaxation of the SBs in 1,4-DOX and DMF (the graphics are presented in Fig. S9 and S10 in the ESI)

Compound	1,4-DOX			DMF		
	R [%]	$k_{1/2}$ [s^{-1}]	$t_{1/2}^a$ [s]	R [%]	k [s^{-1}]	$t_{1/2}^a$ [s]
$E \rightarrow Z$ SB1	53	$5.0 \times 10^{-2} \pm 0.002$	14	61	$6.1 \times 10^{-2} \pm 0.002$	11.5
$Z \rightarrow E$ SB1	—	$5.1 \times 10^{-2} \pm 0.001$	13.5	—	Stable ^b	—
Enol \rightarrow keto SB2	—	—	—	37	$6.3 \times 10^{-2} \pm 0.002$	11
Keto \rightarrow enol SB2	—	—	—	—	Stable ^b	—
$E \rightarrow Z$ SB3	54	$1.9 \times 10^{-2} \pm 0.0003$	36	44	$8.4 \times 10^{-2} \pm 0.002$	8.4
$Z \rightarrow E$ SB3	—	$1.5 \times 10^{-2} \pm 0.0005$	46	—	Stable ^b	—
$E \rightarrow Z$ SB4	34	$4.6 \times 10^{-2} \pm 0.008$	15	16	$2.8 \times 10^{-2} \pm 0.0009$	24
$Z \rightarrow E$ SB4	—	$6.4 \times 10^{-2} \pm 0.002$	11	—	Stable ^b	—

^a Determined by $\frac{\ln 2}{k} = t_{1/2}$. ^b Estimated at RT up to 60 min.

conversion are higher in DMF compared to the 1,4-DOX excluding **SB4** for which the opposite relationship is observed. Thermal relaxation in the nonpolar solvent is faster for **SB1** and **SB3** compared the E/Z photoconversion. The obtained kinetic results indirectly support the DFT calculations using solvation in DMF and the NCIs existing in the Z -isomers, which make them relatively more stable at RT. Our earlier investigation on structurally similar SBs containing 5,5'-dimethylhydantoin rings has shown the same stability of Z -isomers at PSS in DMF.³⁹ Another previous study on the photoswitching performance of 5,5'-dimethyl- and 5,5'-diphenylhydantoin SBs containing 2-hydroxy-1-naphthaldehyde and 1-naphthaldehyde moieties in acetonitrile has shown full recovery to the E -isomers up to 110 min, which is one hundred times slower compared to the faster photoinduced E/Z isomerization to PSS up to 60 s.⁴⁹ This allows us to draw important conclusions related to the solvent-driven photochromic behavior of the studied SBs: (i) in 1,4-DOX, **SB1**, **SB3** and **SB4** behave as T-type photoswitches, because the Z -isomer is unstable and rapidly reverts to the more thermodynamically stable E -isomer; (ii) in DMF, all SBs display P-type photochromism which is related to the similar stabilities of the isomers (bistable system); (iii) 5,5'-disubstituted patterns in the hydantoin ring do not play an important role in their switching behavior. Azomethine aromatic species plays the key role in forming weak NCIs with hydantoin rings in polar solvents. These interactions are unfavorable in nonpolar solvents and lead to fast Z/E thermal relaxation.

Through TDDFT vertical electron transition analysis using IEFPCM in DMF of E - and Z -isomers and enol and keto tautomers, it is possible to obtain a picture of the nature of these transitions in experimental absorption bands before UV-illumination and at PSS (Fig. 6 and Table 6). The experimental bands have a reasonable fitting with theoretical TDDFT analysis and further analysis of the oscillator strength of the transitions by the HOMO and LUMO orbitals indicates that in the most cases longest wavelength transitions are attributed to the direct HOMO \rightarrow LUMO ($S_0 \rightarrow S_1$) excitation. Other shorter wavelength transitions are indirect and mainly come from deeper HOMO levels to the LUMO one. For the keto tautomer of **SB2**, special attention must be paid to its longest wavelength transition at 388 nm, which is

far away from the experimental spectrum at PSS compared to the excellent fitting of the experimental and TDDFT analysis of the enol tautomer (Fig. 6B1, B2 and Table 6). Photoinduced enol/keto tautomerization proceeds *via* excited state intramolecular proton transfer (ESIPT), which is common for the 2-hydroxy substituted SBs.^{60,62} The quantitative and qualitative evaluation can be carried out by fluorescence spectroscopy using excitation and emission bands (Fig. 7). By earlier development methods by L. Antonov and co-workers, it is possible to estimate the efficiency conversion of enol into keto form η_T (for more details see the Experimental section).⁶⁰ In DMF the red-shifted emission at 483 nm is characterized by a large Stokes shift ($\Delta\bar{\nu}$ 9780 cm^{-1}) that indicates keto emission compared to the enol long wavelength UV-emission in 1,4-DOX at 371 nm and a small Stokes shift ($\Delta\bar{\nu}$ 3720 cm^{-1}) (Fig. 7B). The excitation spectrum in DMF exhibits a broad split long wavelength keto band at 388 nm compared to the absorption one. The η_T was calculated approximately to be 71% and the excitation band for keto tautomer is fitted with the TDDFT at 388 nm. Obviously, the excitation spectrum in 1,4-DOX does not show keto excitation and emission and its ESIPT is fairly low. The results correspond to our previous study of 2-hydroxy-1-naphthyl substituted SBs in the various solvents.⁴⁹ In general, the enol emission becomes after excitation to the S_1 state namely locally excited (LE) state. If the ESIPT produces lower energy keto state (S_1^*) compared to the LE one the red-shifted keto ($S_1^* \rightarrow S_0^*$) emission is observed (Fig. 7C). If the keto state is higher in energy compared to the LE one the ESIPT is unlikely and mainly enol emission is dominated. The optimized structures of both tautomers in the S_1 excited state using solvation in DMF and 1,4-DOX support the experimental observation, where the keto state (S_1^*) in DMF is lower in energy compared to the energy of the enol state (S_1) and the ESIPT is observed. In contrast, the energy of the keto state (S_1^*) in 1,4-DOX is much higher than that of the S_1 enol state and the ESIPT is unfavorable (Fig. 7D and E). This demonstrates another spectral approach to the studied **SB2** containing the salicylic moiety, which provides evidence for the solvent dependence bidirectional switching *via* the excited state. The variation of the solvent environment from nonpolar to polar leads to the direct change of the bidirectional switching behaviour from T-type to P-type (Scheme 2). This gives the

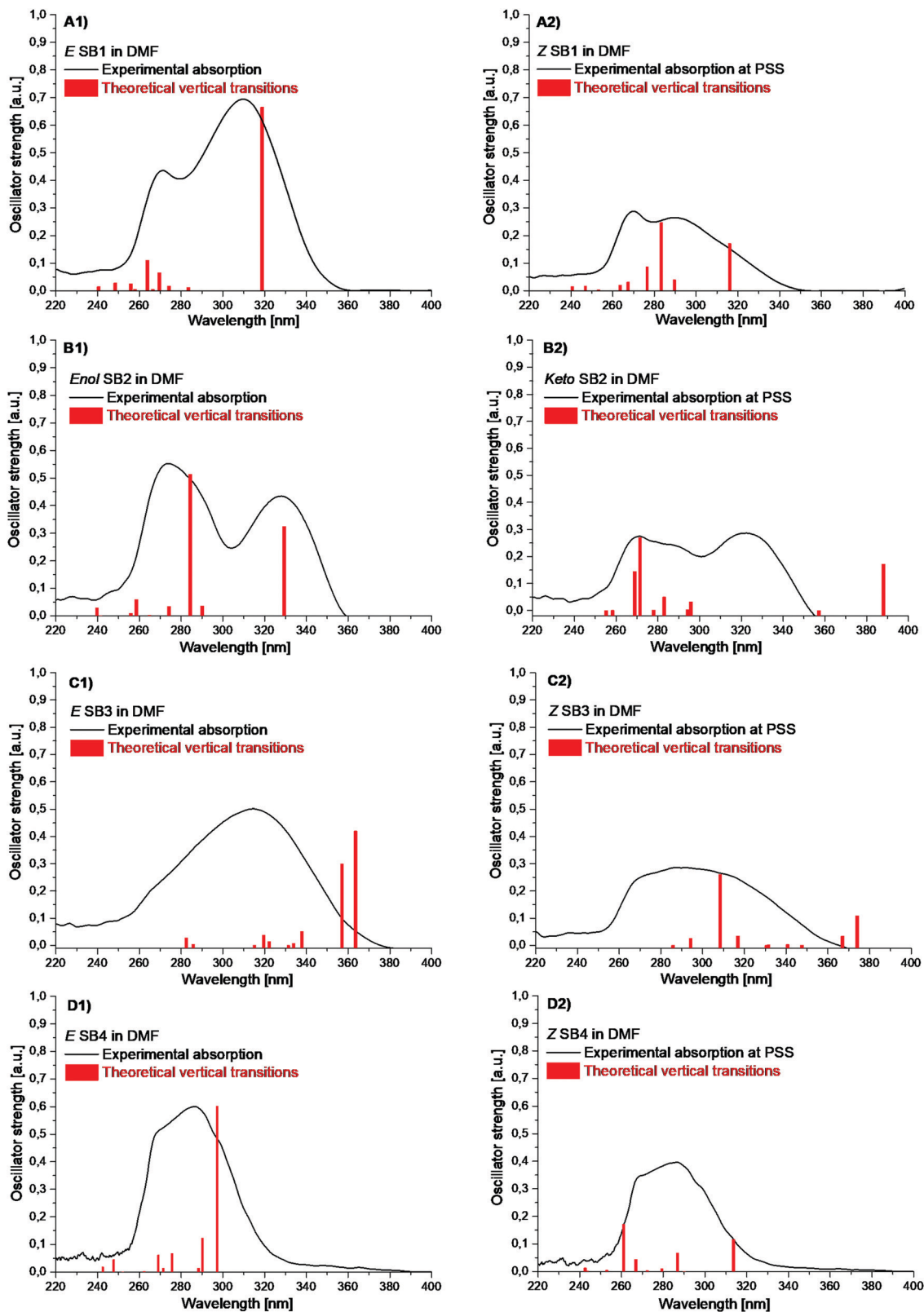


Fig. 6 Experimental absorption and vertical TDDFT electron transitions in DMF of the SBs before UV-illumination (A1, B1, C1 and D1) and at PSS (A2, B2, C2 and D2).

Table 6 Summarized results of absorption wavelengths of the studied SBs before UV-illumination and at PSS. Vertical TDDFT electron transitions using IEFCM in DMF as *E/Z*-isomers and enol/keto tautomers

Compound	Experiment in 1,4-DOX λ_{\max} [nm]	Experiment in DMF λ_{\max} [nm]	TDDFT solvation in DMF λ_{\max} [nm]
<i>E</i> -SB1	314	310	319 (H → L) 263 (H-2 → L)
<i>Z</i> -SB1	312 at PSS	291 at PSS	316 (H-1 → L) 282 (H-2 → L)
Enol-SB2	326	328	329 (H → L) 284 (H-1 → L)
Keto-SB2	—	321 at PSS	388 (H → L) 271 (H-3 → L)
<i>E</i> -SB3	315	314	363 (H → L) 356 (H-1 → L)
<i>Z</i> -SB3	313 at PSS	285 at PSS	374 (H-1 → L) 308 (H-3 → L)
<i>E</i> -SB4	326	286	297 (H → L) 290 (H-1 → L)
<i>Z</i> -SB4	320 at PSS	284 at PSS	313 (H-1 → L) 260 (H → L)

possibility of gaining control over the thermodynamically unstable isomers/tautomers between the two switched states.

3.4. Electrochemical study

Further investigation was carried out on the electrochemical behavior of SBs before and after illumination with UV-light at the PSS in order to evaluate the influence of the irradiation on the intramolecular structure and to show the mechanism of electron exchange in the redox processes. The reduction of *E*- and *Z*-isomer dimethylhydantoin Schiff bases on Pt-electrodes in DMF was discussed in our previous study.³⁹ The voltammograms under the same conditions were also recorded with phenytoin SBs. It was found that the change of the substituent in the hydantoin ring does not affect the reduction of azomethine groups of aromatic moieties. To evaluate the effect of the solvent on the electron exchange in the redox reactions of the SBs, voltammetric studies were carried out in various electrolyte solutions. According to Lai-Hao *et al.*⁶⁹ compounds containing azomethine groups show well-formed reduction peaks in a LiOH/LiCl medium at a mercury electrode. Fig. 8 shows a comparative reduction of the azomethine bond from SB1 at the mercury electrode (HMDE) in three electrolytic media (DMF, MeOH, and LiOH/LiCl (pH 12.21)) with increasing polarities as follows: DMF < MeOH < LiOH. It was observed that the SB1 in DMF produces a very low intense peak at ≈ -0.250 V corresponding to the reduction of the

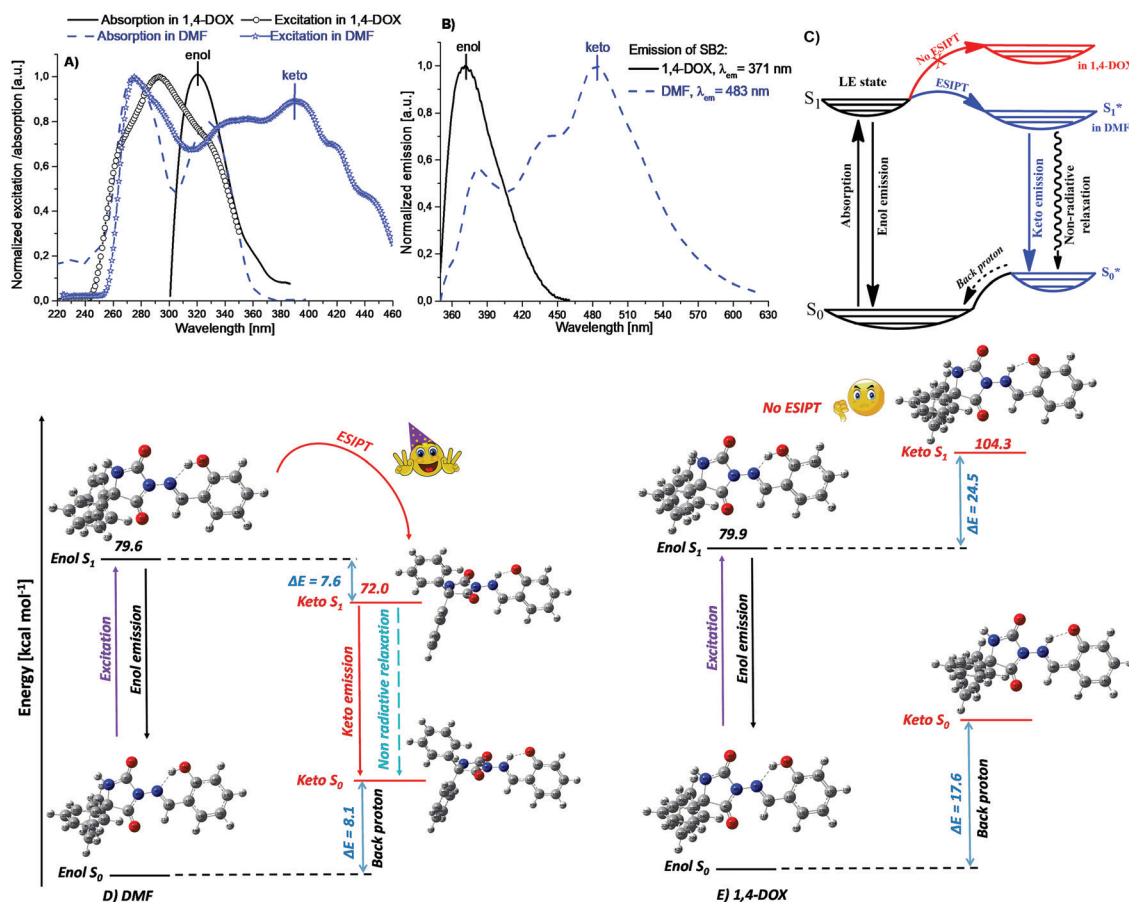
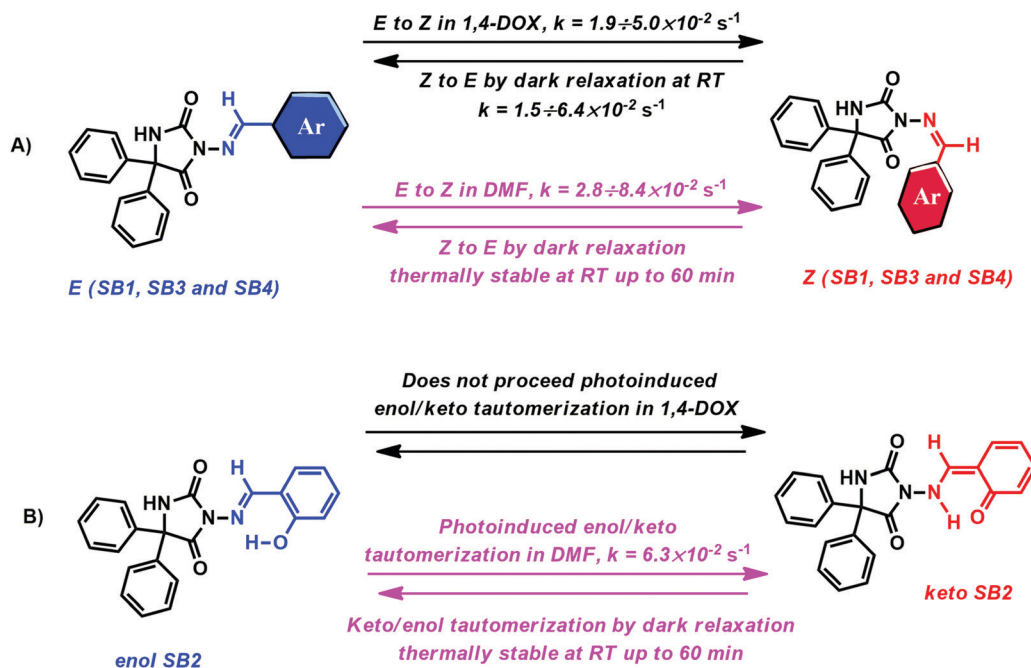


Fig. 7 Absorption/excitation spectra of SB2 in 1,4-DOX and DMF (A), the emissions in the same solvents (B) and the mechanisms of fundamental fluorescence bands by ES IPT and local excitation according to the Jablonski diagram depending on the solvent environment (C). The excitation wavelengths were set to 326 nm (1,4-DOX) and 328 nm (DMF). Optimized structures of enol and keto tautomers in the S_1 excited state by TDDFT B3LYP/6-311+G(2d,p) level of theory using IEFCM in DMF and 1,4-DOX (D and E).



Scheme 2 General concept of the solvent dependence bidirectional photoswitching behavior of the studied SBs: (A) *E/Z* isomerization upon long wavelength UV-light at 350 nm and *Z/E* dark relaxation at RT in 1,4-DOX and DMF; (B) photoinduced enol/keto tautomerization of **SB2** in both solvents.

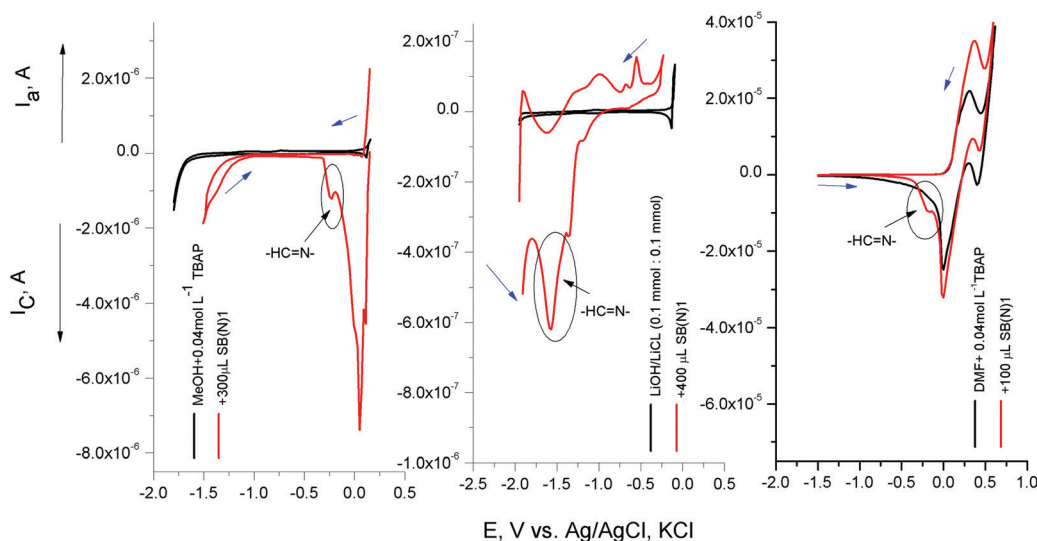


Fig. 8 CVs of 3-amino-5,5'-diphenylhydantoin Schiff base (**SB1**, $2.41 \times 10^{-4} \text{ mol L}^{-1}$) before UV-illumination in three electrolytic media (DMF, MeOH, and LiOH/LiCl (pH 12.21)) at working electrode: hanging mercury drop electrode (HMDE) and scan rate 100 mV s^{-1} .

–CH=N– group (Fig. 8) which is partially overlapped with the current peak of electrolyte background. Three partially overlapped peaks are observed at reduction of the azomethine group of investigated SBs in MeOH. In contrast, well-formed peaks at $\approx -1.5 \text{ V}$ in the proton electrolyte medium (LiOH/LiCl) were obtained corresponding to the reduction of this group.⁶⁹ Therefore, the electrochemical properties of the studied **SB1**–**SB4** were examined in a protic solvent using cyclic (CV) and square wave (SW) voltammetric techniques and the oxidation–reduction peak potentials belonging to potential–current voltammograms

of compounds are given in Fig. 9 and Fig. S11 (ESI[†]). One can find in the literature hesitant opinions about the electrochemical behavior of the hydantoin ring. Some authors have shown that phenytoin cannot be reduced polarographically, while others report that anode waves can be detected under certain conditions.⁷⁰ Under the present conditions, peaks corresponding to the electron exchange of phenytoin in the alkaline medium with the electrode space were not detected.

All SBs show the ease of reduction on the basis of the E_p values of the –CH=N– bond in the following order

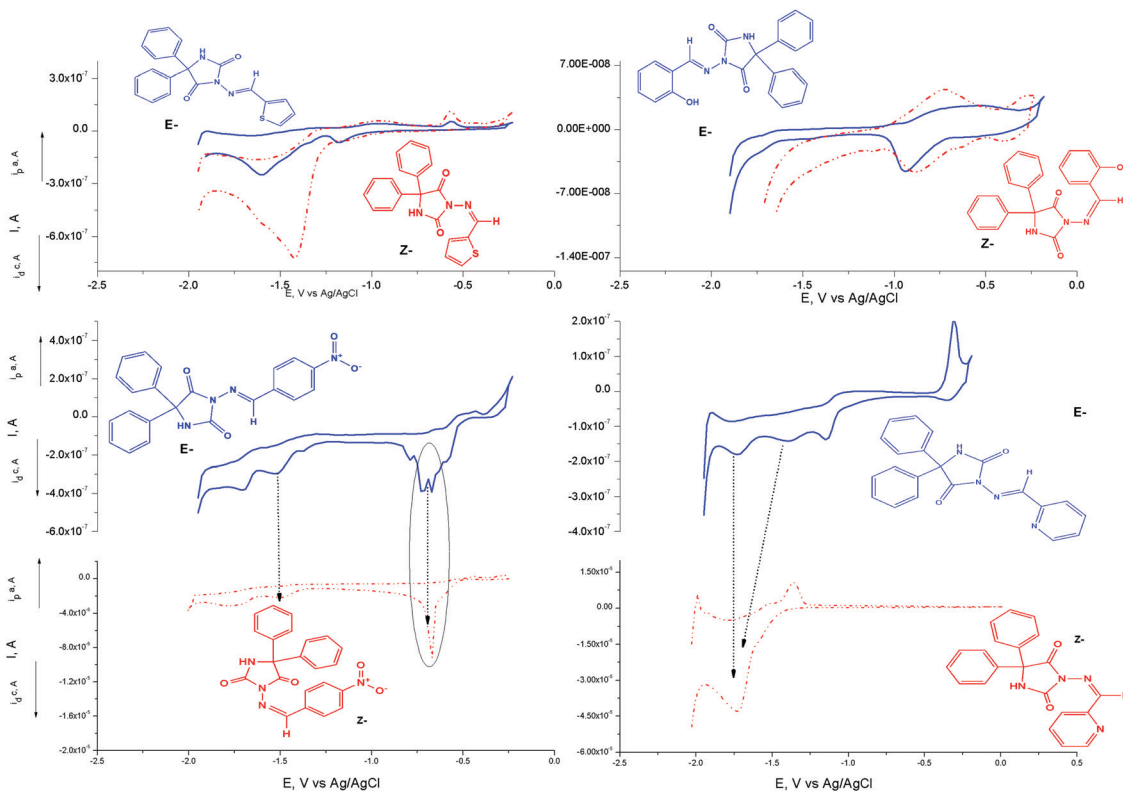


Fig. 9 CVs of 3-amino-5,5'-diphenylhydantoin Schiff bases before (SB(N)) and after (SB(IRr)) UV-illumination at approximately same concentration (SB1: 2.41×10^{-4} ; SB2: 1.66×10^{-4} ; SB3: 1.69×10^{-4} ; SB4: 1.90×10^{-4} mol L $^{-1}$) in LiOH/LiCl (pH = 12.21) at working electrode: hanging mercury drop electrode (HMDE); scan rate 100 mV s $^{-1}$.

SB2 > SB1 > SB4 > SB3 which may be due to the nature of the substituents in the corresponding aldehydes. The cathodic peak potential values of SBs reveal that the reduction potential of the electrophore can be modulated by changing the electronic properties of the substituents attached at the corresponding aromatic rings. This is likely to be due to a decrease in the electrophilicity at the reaction center ($-\text{CH}=\text{N}-$), which inhibits the migration of electrons in the molecule. This also explains

the fact that the electronic uptake reaction for performing the reduction process in the azomethine group of SB3 and SB4 takes place in two stages (Fig. 9). In addition the facile oxidation of SB2 is attributed to the electron-donating effect of the $-\text{OH}$ group (Fig. 9). In order to investigate the electrochemical behavior of E/Z conversion, the SBs were UV-irradiated at $\lambda = 350$ nm by light that was perpendicularly directed to the cuvette containing the samples for 600 s. The cyclic voltammograms

Table 7 Voltamperometric characteristics of the 3-amino-5,5'-diphenylhydantoin Schiff bases (SB1, SB2, SB3, and SB4) in LiOH/LiCl (pH 10.65) before (SB 1–4) and after (SB(IRr) 1–4) UV illumination with $\lambda = 350$ nm at concentrations: SB1: 2.41×10^{-4} ; SB2: 1.66×10^{-4} ; SB3: 1.69×10^{-4} ; SB4: 1.90×10^{-4} mol L $^{-1}$ and scan rate 100 mV s $^{-1}$

Ar-	$-E_{\text{pc}}$, V		$-E_{\text{pa}}$, V		$-I_{\text{pc}}$, nA		I_{pa} , μA		$\Delta E_{\text{pc}} = E_{\text{pc}} - E_{\text{p1/2}}$, mV		$\alpha^a n k^0$, cm s $^{-1}$		$\alpha^a n k^0 \times 10^{-3}$ cm s $^{-1}$ in DMF ⁵⁰	
	N	IRr	N	IRr	N	IRr	N	IRr	N	IRr	N	IRr	N	IRr
	1.59	1.43	1.35	1.91	133	619	91.6	101	10	17	16.2×10^{-3}	1.41×10^{-3}	0.319	2.77
	0.983	0.891	0.691	0.751	40.8	24	12.2	23	15	23	7.82×10^{-6}	2.70×10^{-6}	1.03	0.0740
	0.651	0.661	0.453	—	—	673	—	—	—	—	—	—	—	—
	1.49	1.04	—	0.961	38	16.1	23.7	31.6	16	23	9.40×10^{-5}	11.4×10^{-5}	4.65	1.43
	0.331	0.651	0.311	—	89.6	66.6	35.7	—	—	—	—	—	—	—
	1.13	—	1.01	—	50.7	—	154	—	15	12	6.66×10^{-6}	84.9×10^{-3}	—	—
	1.39	—	—	—	17.4	—	—	—	—	—	—	—	—	—
	1.73	1.71	—	1.37	32.5	25 100	0.112	20 200	—	—	—	—	—	—

^a α coefficient at a quasi-reversible and irreversible systems.

(CVs) at similar concentrations and 100 mV s^{-1} scan rates are also shown in Fig. 9. As can be seen, there is a difference in the type of voltammograms of the compounds under UV-illumination. A change in the current intensity and the potential shifting of the reduction peaks for Z- or keto forms was observed after illumination proving that the type of isomerization affects the electrochemical behavior of the investigated compounds. The azomethine group in **SB2** and **SB3** becomes more easily reduced (E_p is slightly shifted in the positive potential direction) and the current sensitivity increases in the order **SB1** > **SB2**. Moreover, an anode peak is observed for **SB2**, with an $I_{pc}/I_{pa} \approx 1$ and $\Delta E_p (E_{p,c} - E_{p,a}) \approx 100 \text{ V}$, suggesting a quasi-reversible nature of the electrode process (Table 7). It was proved

that in the case of the introduction of the $-\text{OH}$ group at the *ortho*-position, the negative shift of peak potential ($E_{p(c)2}$) takes place, because of the electron donor effect.⁷¹ The square wave (SW) technique demonstrates the complete reversibility of the electrode process for **SB2** and **SB1** and a quasi-reversible electrode reaction for **SB4** (Fig. 9 and Fig. S11, ESI[†]). The two voltammetric techniques (CV and SW) showed no change in the type of electrode reaction at **SB3** (Fig. 9 and Fig. S11, ESI[†]). Only the current decreases dramatically upon irradiation, which indicates a decrease in the reactivity of the molecules. Following the above, it can be concluded that, after energy quanta irradiation, the stability of the compounds in terms of electron exchange in the redox reaction increases as follows: **SB2** > **SB1** > **SB4** > **SB3**.

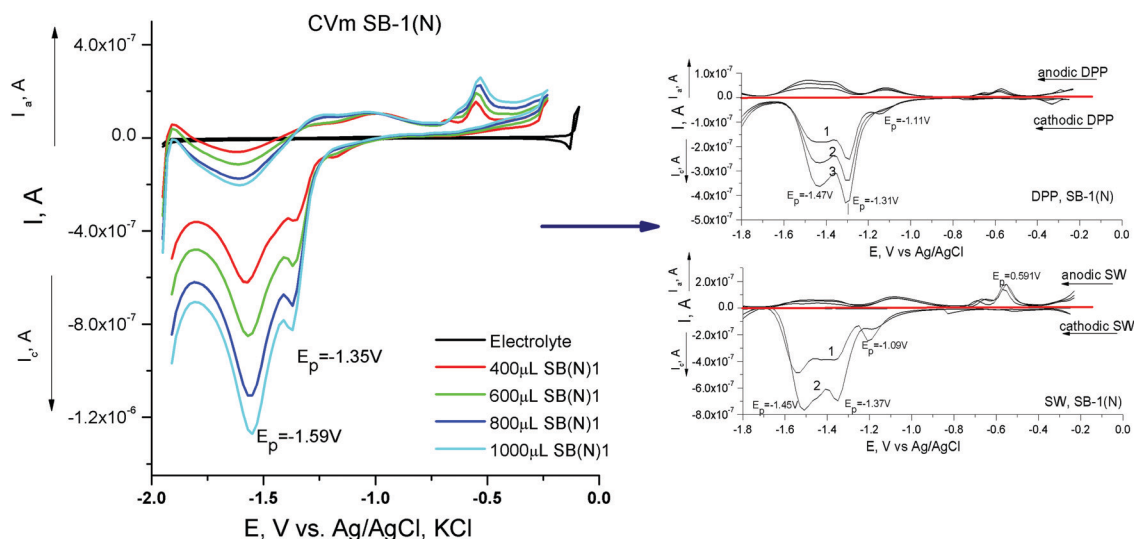


Fig. 10 Voltamperograms of 3-amino-5,5'-diphenylhydantoin Schiff base (**SB1**: 2.41×10^{-4}) before UV-illumination at different modes (CV, SW and DPP) in LiOH/LiCl (pH = 12.21) at working electrode: hanging mercury drop electrode (HMDE); CVs scan rate 100 mV s^{-1} , SW 50 Hz.

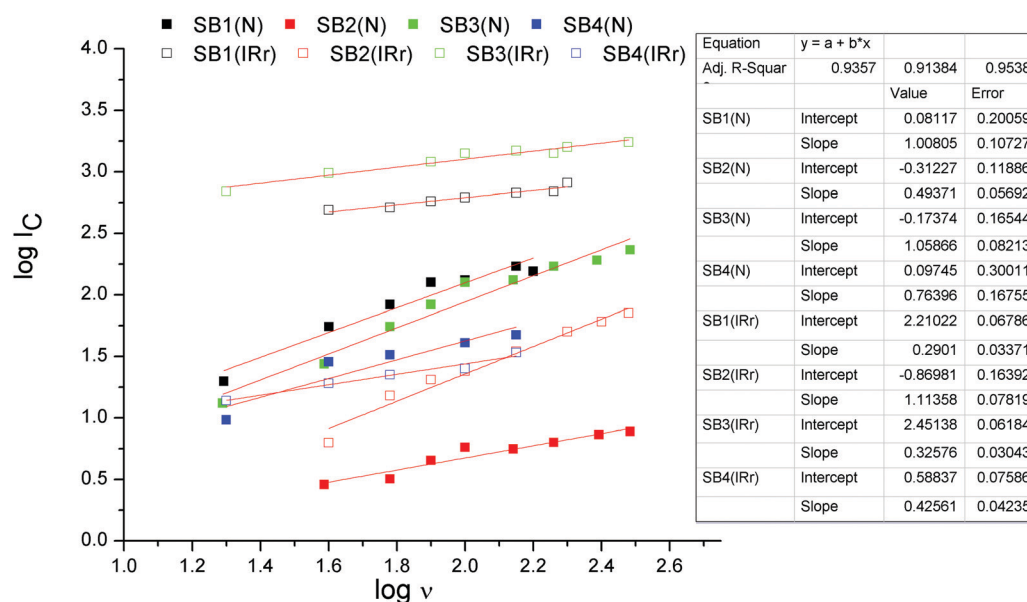
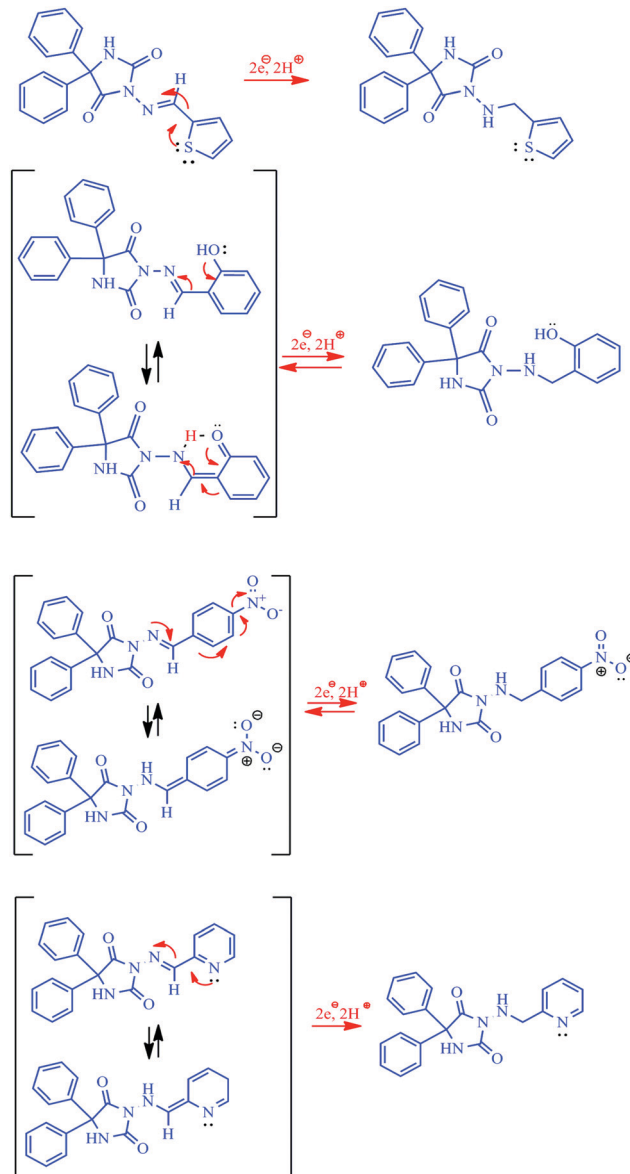


Fig. 11 Plot of cathodic peak high, $\log I_{pc}$ nA vs. logarithmic value of scan rate, $\log \nu$ mV s^{-1} in the range from 20 to 300 mV s^{-1} .

The distance between Epc and half potential value $E_{pc/2}$ ($\Delta E_p = (E_{pc} - E_{pc/2})$) was found to be between 10 and 23 mV for the SBs without (SB(N)) and with irradiation (SB(IRr)) (Table 7) and the ratio of peak heights I_{pc}/I_{pa} is greater than one, suggesting the reversible or quasi-reversible nature of the reaction of the electrochemical reduction process.⁷² For all compounds, a linear change in the current height with an increase in the concentration was registered. The voltamperograms for **SB1** at different modes (CV, DPP and SW) are presented in Fig. 10. A proportional relationship between the current and concentration is also observed in analyzes with differential pulse polarography (DPP) and SWV (Fig. 10), which indicate that radical cations, reduction products of the investigated compounds, are adsorbed on the electrode surface. Kinetic data are shown in Table 7 and are plotted in Fig. S12 (ESI†). The values of the heterogeneous rate constant (k^0) are calculated using the Reimuth expression, $I_{pc} = nFAc^0k^0$, given in the literature.⁷³ Comparing the values of the investigated SBs with those in the previous study we found that the type of solvent, as well as the working electrode, does not change significantly the value of k^0 for **SB2(N)** and **SB2(IRr)**. A change of the heterogeneous rate constant is observed for all the rest of the SBs as the value of the " k^0 " decreases 100 to 10000 times indicating the lower electron transfer kinetics of compounds and a quasi-reversible to irreversible nature of the electrode reaction. Moreover, the irradiation of the compounds does not have a significant effect on the value of k^0 for **SB1**, **SB2**, and **SB3**. However, the k^0 value increased significantly after irradiation of **SB4** which may be related to the probable compression of the electrical double layer due to isomerization (Table 7). This can be attributed to an increase in the stability of the compound due to the quasi-reversible nature of the redox reaction. The scan rate effect was also monitored for all SBs at a scan rate from 0.2 to 3.0 V s⁻¹ (Fig. S13 and S14, ESI†). The negligible potential shift of the cathodic peak with an increase in the scan rate (ν) predicted the electrochemical process of the compounds to be with reversible nature. We also found that illumination influences the nature of the redox process. A diffusion-controlled nature of the process was found for all illuminated SBs (excepting **SB2**) after plotting $\log I_{pc}$ vs. $\log \nu$ with an increasing value of the slope as follows: **SB1(IRr)** < **SB3(IRr)** < **SB4(IRr)** (Fig. 11). The slope values from 0.71 to 1.0 indicated the adsorption controlled process for **SB1**, **SB3(N)** and **SB4(N)** while the slope value of ~ 0.50 for the **SB2(N)** showed the intermediate (diffusion cum adsorption controlled) nature of the process.⁷⁴

The controlled potential electrolysis technique (coulometry) with a mercury pool cathode was used for the total number of electron determination involved in the electrode reaction by applying the equation: $Q = nFw/M$ (where w is the weight of the sample (in grams), M is its molecular weight, and F – Faraday constant). The accumulated charge (Q) was read at a potential corresponding to the current peak of the voltammogram. Based on coulometric data (Table 2), it can be concluded that the electro-reduction process for SBs is carried out by the addition of 2 electrons and 2 protons to the $-\text{CH}=\text{N}-$ center and the corresponding reduction of the azomethine group in DMF at



Scheme 3 Proposed redox mechanism of Schiff bases 1–4.

the Pt-electrode.³⁹ As an additional cathodic peak at ≈ -0.650 V is observed in the voltammogram of **SB3**, which is attributed to the reduction of $-\text{NO}_2$ group to hydroxyamine ($-\text{NHOH}$), the reduction process of the compounds can be concluded to involve 4 electrons and 4 protons in addition. Summarizing the data from voltamperometry and coulometry, the mechanism of the electrode reaction for the reduction of the $-\text{CN}=\text{N}-$ group can be represented as follows (Scheme 3).

4. Conclusions

A systematical study of four novel Schiff base derivatives of 3-amino-5,5'-diphenylhydantoin containing different aromatic moieties (**SB1**–**SB4**) has been presented. By using combined approaches, experimental and theoretical, the solvent-driven

bidirectional photoswitching behavior has been investigated by optical and electrochemical methods.

Ground state DFT calculations *in vacuo* as *E*-isomers (**SB1**, **SB3** and **SB4**) and enol tautomer (**SB2**) were supported by X-ray analysis, where near planar conformation around $-\text{CH}=\text{N}-$ bonds has been observed. The *Z*-isomers are characterized by twisting conformation with a $\text{C}_{10}-\text{N}_9-\text{N}_8-\text{C}_2$ dihedral angle of $60-80^\circ$ and such a structure suggests near T-shaped conformation forming a weak noncovalent interaction (NCI). The kinetic results in 1,4-DOX display a T-type photoswitch behavior, because the *Z*-isomer (at PSS) is unstable and rapidly reverts to the more thermodynamically stable *E*-isomer at room temperature. The opposite behavior was observed in DMF displaying P-type photochromism related to the similar stabilities of both isomers (bistable system). Azomethine aromatic species plays the key role in forming weak NCIs with hydantoin rings in polar solvents. These interactions are unfavorable in nonpolar solvents and lead to fast *Z/E* thermal relaxation. The obtained kinetic results indirectly support the DFT calculations using solvation in DMF. Special attention was paid to **SB2** in terms of its tautomerism in the ground and excited states by absorption and emission spectroscopies. The optimized structures of both tautomers in the S_1 excited state using solvation in DMF and 1,4-DOX support the experimental observation, where the keto state (S_1^*) in DMF is lower in energy compared to the energy of the enol state (S_1) and the ESIPT is observed by red-shifted keto emission at 483 nm. In contrast, the energy of the keto state (S_1^*) in 1,4-DOX is much higher than that of the S_1 enol state and the ESIPT is unfavorable with a long wavelength UV enol emission at 371 nm. By using different spectral experiments for the **SB2** containing salicylic moieties, the evidence for solvent dependence bidirectional switching *via* the excited state has been provided. The electrochemical behavior of SBs before and after UV-illumination was helpful in estimating the mechanism of electron exchange in the redox processes for *E*- and *Z*-isomers as well as keto and enol tautomers. The results showed that the absorption of energy quanta leads to changes in kinetics data, the type of electrode reaction and the nature of the redox process of the compounds.

The variation of the solvent environment from nonpolar to polar leads to the direct change of the bidirectional switching behaviour from T-type to P-type. This gives the possibility of gaining control over the thermodynamically unstable isomers/tautomers between the two switched states.

Conflicts of interest

The authors declare that they have no conflict of interest.

Acknowledgements

This work was financially supported by the Bulgarian National Scientific Fund project ДН 18/5 "Novel azo materials and application of their photophysical properties as reversible optical storage devices" of the Ministry of Education and Science, Bulgaria. Research equipment of distributed

research infrastructure INFRAMAT (part of Bulgarian National roadmap for research infrastructures) supported by Bulgarian Ministry of Education and Science under contract D01-284/17.12.2019 was used in this investigation.

Notes and references

- 1 A. Bakkar, F. Lafalet, D. Roldan, E. Puyoo, D. Jouvenot, G. Royal, E. Saint-Amanaand and S. Cobo, *Nanoscale*, 2018, **10**, 5436–5441.
- 2 Y. Kim, G. Wang, M. Choe, J. Kim, S. Lee, S. Park, D. Kim, B. Hun and T. Lee, *Org. Electron.*, 2011, **12**, 2144.
- 3 S. Kobatake, S. Takami, H. Muto, T. Ishikawa and M. Irie, *Nature*, 2007, **446**, 778.
- 4 Y. Tsuji and R. Hoffmann, *Angew. Chem., Int. Ed.*, 2014, **53**, 4093.
- 5 G. Berkovic, V. Krongauz and V. Weiss, *Chem. Rev.*, 2000, **100**, 1741.
- 6 M. F. Brown, G. F. Salgado and A. V. Struts, *Biochim. Biophys. Acta*, 2010, **1798**, 177–193.
- 7 A. Credi, M. Semeraro, S. Silvi and M. Venturi, *Antioxid. Redox Signaling*, 2011, **14**, 1119–1165.
- 8 V. Balzani, A. Credi and M. Venturi, *Molecular Devices and Machines: Concepts and Perspectives for the Nanoworld*, Wiley-VCH Verlag, Germany, Weinheim, Germany, 2008.
- 9 V. Balzani, A. Credi and M. Venturi, *Nano Today*, 2007, **2**, 18–25.
- 10 M. Dong, A. Babalhavaeji, S. Samanta, A. A. Beharry and G. A. Woolley, *Acc. Chem. Res.*, 2015, **48**, 2662–2670.
- 11 E. Darko, P. Heydarizadeh, B. Schoefs and M. R. Sabzalian, *Philos. Trans. R. Soc., B*, 2014, **369**, 20130243.
- 12 M. Blanco-Lomas, I. Funes-Ardoiz, P. Campos and D. Sampedro, *Eur. J. Org. Chem.*, 2013, 6611–6618.
- 13 C. Garcia-Iriepa, M. Marazzi, L. M. Frutos and D. Sampedro, *RSC Adv.*, 2013, **3**, 6241–6266.
- 14 S. Patai, *The Chemistry of the carbon-nitrogen double bond*, John Wiley & Sons Ltd., London, 1970.
- 15 M. D. Shelley, L. Hartley, P. W. Groundwater and R. G. Fish, *Anti-Cancer Drugs*, 2000, **11**, 209.
- 16 P. Przybylski, W. Schilf, B. Kamiński, B. Brzezinski and F. Bartl, *J. Mol. Struct.*, 2005, **748**, 111.
- 17 P. Przybylski, F. Bartl and B. Brzezinski, *Biopolymers*, 2002, **65**, 111.
- 18 P. Przybylski, M. Małuszyńska and B. Brzezinski, *J. Mol. Struct.*, 2005, **750**, 152–157.
- 19 D. Kong, X. Zhang, Q. Zhu, J. Xie and X. Zhou, *Zhongguo Yaowu Huaxue Zazhi*, 1998, **8**, 245.
- 20 D. J. Hadjipavlou-litina and A. A. Geronikaki, *Drug Des. Discovery*, 1996, **15**, 199.
- 21 S. J. Wadher, M. P. Puranik, N. A. Karande and P. G. Yeole, *Int. J. PharmTech Res.*, 2009, **1**, 22.
- 22 A. L. Cates and S. M. Rasheed, *Pharm. Res.*, 1984, **6**, 271.
- 23 S. K. Sridhar, S. N. Pandeya, J. P. Stables and A. Ramesh, *Eur. J. Pharm. Sci.*, 2002, **16**, 129–132.
- 24 I. Saadaoui, F. Krichen, B. B. Salah, R. B. Mansour, N. Miled, A. Bougatef and M. Kossentini, *J. Mol. Struct.*, 2019, **1180**, 344–354.

- 25 K. Tanaka, R. Shimoura and M. R. Caira, *Tetrahedron Lett.*, 2010, **51**, 449–452.
- 26 G. Pistolis, D. Gegiou and E. Hadjoudis, *J. Photochem. Photobiol., A*, 1996, **93**, 179–184.
- 27 Y. M. Issa, O. E. Sherif and S. M. Abbas, *Monatsh. Chem.*, 1998, **129**, 985–998.
- 28 A. M. Atta, N. O. Shaker and N. E. Maysour, *Prog. Org. Coat.*, 2006, **56**, 100–110.
- 29 J. H. Jia, X. M. Tao, Y. J. Li and W. J. Sheng, *Chem. Phys. Lett.*, 2011, **514**, 114–118.
- 30 L. Konnert, F. Lamaty, J. Martinez and E. Colacino, *Chem. Rev.*, 2017, **117**, 13757–13809.
- 31 M. Lupacchini, A. Mascitti, L. Tonucci, N. d'Alessandro, E. Colacino and C. Charnay, *ACS Sustainable Chem. Eng.*, 2018, **6**, 511–518.
- 32 E. Colacino, A. Porcheddu, I. Halasz, C. Charnay, F. Delogu, R. Guerra and J. Fullenwarth, *Green Chem.*, 2018, **20**, 2973–2977.
- 33 L. Somsak, V. Nagy, Z. Hadady, N. Felfold, T. Docsa and P. Gergely, *Front. Med. Chem.*, 2005, **2**, 253.
- 34 P. Todorov, E. Naydenova and K. Troev, *Heteroat. Chem.*, 2009, **20**(2), 87–90.
- 35 E. Naydenova, P. Todorov and K. Troev, *Phosphorus, Sulfur Silicon Relat. Elem.*, 2010, **185**(7), 1315–1320.
- 36 P. Todorov, O. Aneva and E. Naydenova, *Heteroat. Chem.*, 2011, **22**(5), 669–672.
- 37 S. Georgieva, P. Todorov and D. Wesselinova, *C. R. Chim.*, 2014, **17**, 1212–1220.
- 38 P. Todorov, R. Petrova, E. Naydenova and B. Shivachev, *Cent. Eur. J. Chem.*, 2009, **7**, 14–19.
- 39 P. T. Todorov, P. N. Peneva, S. I. Georgieva, R. I. Rusew, B. Shivachev and A. Georgiev, *New J. Chem.*, 2019, **43**, 2740–2751.
- 40 P. J. Coelho, M. Cidália, R. Castro, M. Manuela and M. Raposo, *J. Photochem. Photobiol., A*, 2013, **259**, 59–65.
- 41 Y. Luo, M. Utecht, J. Dokić, S. Korchak, H. M. Vieth, R. Haag and P. Saalfrank, *ChemPhysChem*, 2011, **12**, 2311–2321.
- 42 A. Georgiev, A. Kostadinov, D. Ivanov, D. Dimov, S. Stoyanov, L. Nedelchev, D. Nazarova and D. Yancheva, *Spectrochim. Acta, Part A*, 2018, **192**, 263–274.
- 43 P. J. Coelho, M. Cidália, R. Castro, M. Manuela and M. Raposo, *J. Photochem. Photobiol., A*, 2013, **259**, 59–65.
- 44 Q. Wang, L. Cai, F. Gao, Q. Zhou, F. Zhan and Q. Wang, *J. Mol. Struct.*, 2010, **977**, 274–278.
- 45 H. L. Saadon, B. Ali and A. A. Al-Fregi, *Opt. Laser Technol.*, 2014, **58**, 33–38.
- 46 K. Kiec-Kononowicz, A. Zejc and H. Byrtus, *Pol. J. Chem.*, 1984, **58**, 585–591.
- 47 A. Ashnagar, N. Gharib Naseri and M. Amini, *Asian J. Chem.*, 2009, **21**, 4976–4980.
- 48 S. M. D. Al-Nuzal, M. F. Al-Dulaimi and A. T. Hassan, *Journal of University of Anbar for Pure Science*, 2018, **12**, 38–53.
- 49 A. Georgiev, P. Todorov and D. Dimov, *J. Photochem. Photobiol., A*, 2020, **386**, 112143.
- 50 G. M. Sheldrick, *Acta Crystallogr., Sect. A: Found. Crystallogr.*, 2008, **64**, 112–122.
- 51 L. Farrugia, *J. Appl. Crystallogr.*, 2015, **45**, 849–854.
- 52 C. F. Macrae, P. R. Edgington, P. McCabe, E. Pidcock, G. P. Shields, R. Taylor, M. Towler and J. van de Streek, *J. Appl. Crystallogr.*, 2006, **39**, 453–457.
- 53 M. J. Frisch, G. W. Trucks, H. B. Schlegel, G. E. Scuseria, M. A. Robb, J. R. Cheeseman, G. Scalmani, V. Barone, B. Mennucci, G. A. Petersson, H. Nakatsuji, M. Caricato, X. Li, H. P. Hratchian, A. F. Izmaylov, J. Bloino, G. Zheng, J. L. Sonnenberg, M. Hada, M. Ehara, K. Toyota, R. Fukuda, J. Hasegawa, M. Ishida, T. Nakajima, Y. Honda, O. Kitao, H. Nakai, T. Vreven, J. A. Montgomery Jr, J. E. Peralta, F. Ogliaro, M. Bearpark, J. J. Heyd, E. Brothers, K. N. Kudin, V. N. Staroverov, T. Keith, R. Kobayashi, J. Normand, K. Raghavachari, A. Rendell, J. C. Burant, S. S. Iyengar, J. Tomasi, M. Cossi, N. Rega, J. M. Millam, M. Klene, J. E. Knox, J. B. Cross, V. Bakken, C. Adamo, J. Jaramillo, R. Gomperts, R. E. Stratmann, O. Yazyev, A. J. Austin, R. Cammi, C. Pomelli, J. W. Ochterski, R. L. Martin, K. Morokuma, V. G. Zakrzewski, G. A. Voth, P. Salvador, J. J. Dannenberg, S. Dapprich, A. D. Daniels, O. Farkas, J. B. Foresman, J. V. Ortiz, J. Cioslowski and D. J. Fox, *Gaussian 09, Revision D.01*, Gaussian, Inc., Wallingford CT, 2013.
- 54 Y. Luo, M. Utecht, J. Dokić, S. Korchak, H. M. Vieth, R. Haag and P. Saalfrank, *ChemPhysChem*, 2011, **12**, 2311–2321.
- 55 A. Airinei, N. Fifere, M. Homocianu, C. Gaina, V. Gaina and B. C. Simionescu, *Int. J. Mol. Sci.*, 2011, **12**, 6176–6193.
- 56 D. Isac, A. Airinei, M. Homocianu, N. Fifere, C. Cojocaru and C. Hulubei, *J. Photochem. Photobiol., A*, 2020, **390**, 112300.
- 57 K. Bujak, H. Orlikowska, A. Sobolewska, E. Schab-Balcerzak, H. Janeczek, S. Bartkiewicz and J. Konieczkowska, *Eur. Polym. J.*, 2019, **115**, 173–184.
- 58 A. Miniewicz, H. Orlikowska, A. Sobolewska and S. Bartkiewicz, *Phys. Chem. Chem. Phys.*, 2018, **20**, 2904–2913.
- 59 A. Altomare, C. Carlini, F. Ciardelli, R. Solaro, J. L. Houben and N. Rosato, *Polymer*, 1983, **24**, 95–100.
- 60 H. Joshi, F. S. Kamounah, C. Gooijer, G. Van Der Zwan and L. Antonov, *J. Photochem. Photobiol., A*, 2002, **152**, 183–191.
- 61 R. Chavdarova, T. Nedeltcheva and L. Vladimirova, *Anal. Chim. Acta*, 1997, **353**, 325–328.
- 62 L. Antonov, W. M. F. Fabian, D. Nedeltcheva and F. S. Kamounah, *J. Chem. Soc., Perkin Trans. 2*, 2000, 1173–1179.
- 63 J. Calbo, C. E. Weston, A. J. P. White, H. S. Rzepa, J. Contreras-García and M. J. Fuchter, *J. Am. Chem. Soc.*, 2017, **139**, 1261–1274.
- 64 A. Airinei, N. Fifere, M. Homocianu, C. Gaina, V. Gaina and B. C. Simionescu, *Int. J. Mol. Sci.*, 2011, **12**, 6176–6193.
- 65 D. Isac, A. Airinei, M. Homocianu, N. Fifere, C. Cojocaru and C. Hulubei, *J. Photochem. Photobiol., A*, 2020, **390**, 112300.
- 66 K. Bujak, H. Orlikowska, A. Sobolewska, E. Schab-Balcerzak, H. Janeczek, S. Bartkiewicz and J. Konieczkowska, *Eur. Polym. J.*, 2019, **115**, 173–184.
- 67 A. Miniewicz, H. Orlikowska, A. Sobolewska and S. Bartkiewicz, *Phys. Chem. Chem. Phys.*, 2018, **20**, 2904–2913.
- 68 A. Altomare, C. Carlini, F. Ciardelli, R. Solaro, J. L. Houben and N. Rosato, *Polymer*, 1983, **24**, 95–100.

- 69 L.-H. Wang and S.-J. Tsai, *Anal. Chim. Acta*, 2001, **441**, 107–116.
- 70 M. Romer, L. G. Donaruma and P. Zuman, *Anal. Chim. Acta*, 1977, **88**(2), 261–273.
- 71 M. Uehara and J. Nakaya, *Bull. Chem. Soc. Jpn.*, 1970, **43**, 3136–3142.
- 72 S. Georgieva, P. Todorov and E. Naydenova, *Anal. Bioanal. Electrochem.*, 2017, **9**, 214–231.
- 73 A. Shah, A. M. Khan, R. Qureshi, F. L. Ansari, M. F. Nazar and S. S. Shah, *Int. J. Mol. Sci.*, 2008, **9**, 1424.
- 74 E. M. Mabrouk, R. N. Felaly and E. H. El-Mossalamy, *Int. J. Electrochem. Sci.*, 2016, **11**, 4892–4908.